Design and Characterization of an Optical Tweezers System with Adaptive Optic Control

by

Shaun Bowman
B.Eng., University of Victoria, 2007

A Thesis Submitted in Partial Fulfillment
of the Requirements for the Degree of

MASTERS OF APPLIED SCIENCE

in the Department of Mechanical Engineering

Supervisory Committee

Design and Characterization of an Optical Tweezers System with Adaptive Optic Control

by

Shaun Bowman
B.Eng., University of Victoria, 2007

Supervisory Committee

Dr. Colin Bradley, Department of Mechanical Engineering
Supervisor

Dr. Rustom Bhiladvala, Department of Mechanical Engineering
Co-Supervisor or Departmental Member

Dr. Zuomin Dong, Department of Mechanical Engineering
Departmental Member

Abstract

Supervisory Committee

Dr. Colin Bradley, Department of Mechanical Engineering

Supervisor

Dr. Rustom Bhiladvala, Department of Mechanical Engineering

Co-Supervisor or Departmental Member

Dr. Zuomin Dong, Department of Mechanical Engineering

Departmental Member

The thesis details the design and characterization of an innovative optical tweezer system. Optical tweezers provide a relatively new technique for non-contact manipulation of micron-scale particles. They employ a laser beam to hold such particles at the laser's focus. Optical tweezers are used for many scientific purposes, such as: measuring the mechanical properties of bio-molecules, cell and molecule sorting, stiction-less micro-manipulators, and fundamental research in physics. Typically, trap location has been controlled using steer-mirrors or spatial light modulators, operating without beam quality feedback. Here, an innovative trap control system has been developed, featuring a closed-loop adaptive optics system. The prototype system employs a deformable mirror and wavefront sensor to control trap position in three dimensions, while simultaneously removing beam aberrations. The performance of this system is investigated in terms of controllable range of trap motion, trap stiffness, and trap position stability.

Table of Contents

List of Tables

List of Figures

Acknowledgments

I would like to thank some of the great number of people whose support I've enjoyed over the course of my M.A.Sc. program. I would like to thank my supervisor *Dr. Colin Bradley* for his motivation and guidance and for his superlative abilities as a lab director. I would like to thank *Dr. Rodolphe Conan* for being very helpful and generous with his expertise in Adaptive Optics, and for the fantastic library of software tools he has created. I would also like to thank my other lab mates, *Dr. Olivier Lardiere,* and *Dr. Peter Hampton* for helping me with some of the tricky bits of optics and control theory. Still many more people, my friends and loved ones, have helped me to enjoy my time here and provide moral support. Finally, I must express my tremendous thanks and eternal gratitude to my mother *Jean Bowman* and my father *Vic Bowman,* for their unwavering support and encouragement in every step of my life.

Dedication

To my mother,

Jean Bowman

&

my father

Vic Bowman

Chapter 1 - Introduction

Introduction

This thesis details the design and characterisation of a device that can be used to move and apply forces to microscopic particles using a beam of laser light. The device is called an optical tweezer. Optical tweezers are an active field of research having many applications from the study of fundamental physics to biology. The optical tweezer described here is unique because it has an adaptive optic mechanism which simultaneously optimizes the laser beam quality and manipulates the trapped particle position.

Background of Optical Tweezing

Optical tweezing employs a strongly focused laser beam to trap and hold particles such as cells or microscopic transparent beads. The trapped particles are usually suspended in a liquid medium such as water. Trapped objects range in size from 35 nm [1] to over 25 um [2][3], and have an index of refraction larger than the surrounding medium. Optical traps, the parent category of devices to optical tweezers, were originally used to study basic physics. Arthur Ashkin is credited with being the first to study optical trapping, and published a seminal paper in 1970 [4]. In that time, he proposed using the device to create a laser powered pump for gas particles [4]. Later, he worked with Dr Steve Chu who went on to win a Nobel prize for using optical traps to cool atoms to extremely low temperatures. In more recent times, optical traps have become a major research tool for

biophysicists who use them to study small biological objects like cells, DNA, fungi, viruses and bacteria [5][6][3][7]. Optical traps are used to trap these biological samples directly, or, in many cases, the sample is attached to one, or more, larger spheres which are manipulated by the optical trap. For instance, by attaching one end of viral DNA to a trapped sphere, and the other to a receptive trapped cell held stationary by suction or some other means, the displacement of the trapped sphere can be tracked to measure the uptake of the virus [8] . Using an optical tweezer as a force probe of biological processes is a very active research area in biophysics [9]. The forces produced by biomotors often have characteristic magnitudes depending on the chemical reaction, by measuring the forces produced by these motors using an optical trap, the motive chemical process can be identified [10][8] . A depiction of a classical optical tweezer force probe is given in Figure 1.

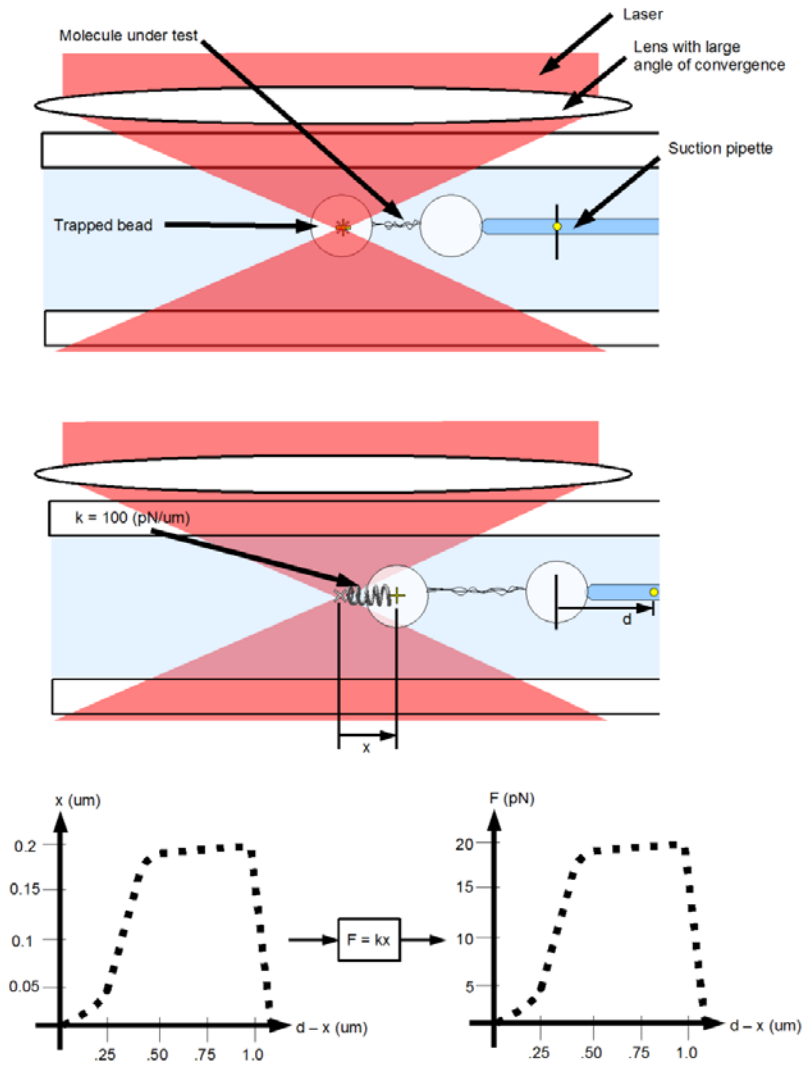

Figure 1 – Optical tweezers are used to measure the response of biological molecules to an applied force. In the top image, a molecule is bound to two spheres. The left sphere is trapped, and the right sphere is held through suction to a pipette. In the middle image, the pipette has been displaced a distance *d* from the rest position. This has caused a smaller displacement *x* of the trapped particle. Through a process of calibration, the resistance applied by the trap to particle displacement has been modeled as a linear spring with stiffness *k* for displacements up to approximately 1/3 the radius of the trapped particle. In the lower-left image, the trapped and bound bead displacements have been determined by analysing video frames. By multiplying *x* displacement by the spring stiffness *k*, the lower-right image shows the force-extension curve of the trapped molecule. [11][12]

Another area of research employs optical tweezers to study biological motors. Alternative small force applying mechanisms to optical tweezers, such as the atomic force microscope, do not have the force-resolution necessary to study biological motors[13]. Such motors have a force range between 1 and 10 pN. Optical Tweezers can produce forces between 0.01 and 200 pN [13]. Examples of biological motors are the linear motor formed by muscle protein's myosin and kinesis; rotary propellers such as bacterial flagella; and jet propulsion such as bacterial gliding. Optical tweezers are currently the most accurate method to quantitatively measure the forces and force-response curves of these motors.

As well as studying biomotors, optical tweezers can be used to measure the viscoelastic properties of proteins [14] , DNA [6], and cells [15]. Biophysicists seek to discover at the mechanical level, how these subtle changes in these components can cause problems in the overall system. The forces required to manipulate these components are on the order of tens of piconewtons and optical traps are currently the technology best suited to study these phenomena.

The above applications of optical tweezing all involve stretching objects using 1-D motion. Increasingly, multiple traps are desirable. There has been recent research activity in the field of multiple trap systems. Employing multiple traps, viscoelastic properties can be studied in two or more dimensions, the individual traps stretching the cell like a sail [16]. In an experiment by Dame et. al., a four-trap system was used to manipulate two

independent DNA molecules[17]. The group used multiple tweezers to show that a protein, H-NS, involved in binding two segments of DNA was only effective when the molecules were first overlapped, and not when H-NS was introduced beforehand. To achieve this independence of motion, active multi-axis control of the position of each trap's light beam is required, the simple pipette in Figure 1 is not sufficient. Another benefit of active control is the resolution of small displacements. Ultimately the sensitivity of an optical trap as a force gauge is limited by the ability to resolve relative motion; because optical forces are calculated by multiplying the trap stiffness by the displacement of a trapped particle from its rest position. Drift in position of the optical elements decreases sensitivity because it affects the trap displacement measurement, so reducing drift is another reason to actively control the trapping beam.

Use of Adaptive Optics for Optical Trapping

Adaptive optics (AO) is principally used as a method for removing the distortion from images, caused by turbulence in the Earth's atmosphere, when viewed by a ground based telescope [18]. AO is a technique that employs a software control system, adaptive optical elements and a beam sensor to remove wavefront errors from the beam, see Figure 2.

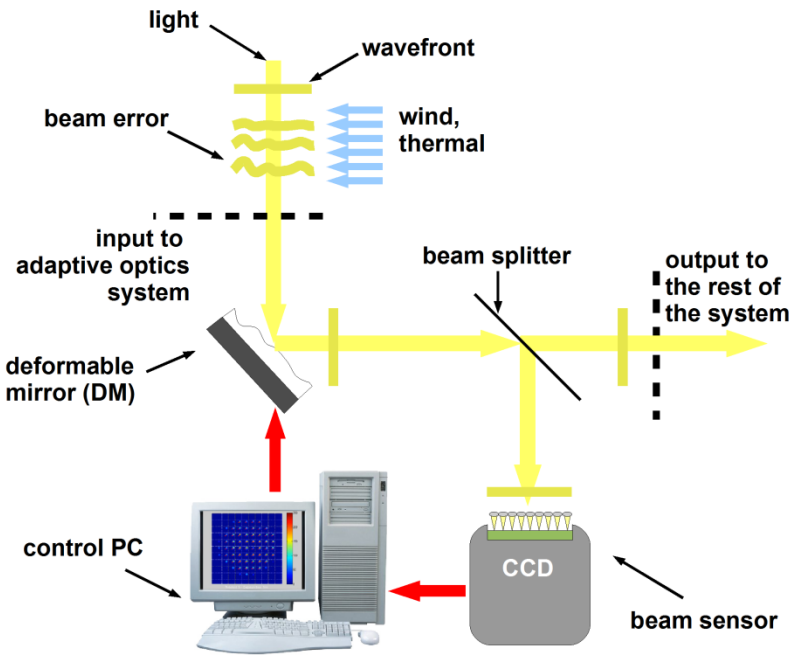

Figure 2- A basic adaptive optics (AO) system uses a software control system to correct for beam error by taking inputs from a beam sensor, and making appropriate adjustments to an adaptive optical element, the deformable mirror (DM).

In this work, adaptive optics is used to control the laser beam of a single trap. Additionally, a proof of concept experiment has also shown that this technique can be converted to a four trap system.

In this experiment, the manipulated optical component is a deformable mirror (DM). A deformable mirror can change shape because it has actuators on its non-reflecting side that are computer controlled. The DM has enough actuators to control the 3-D position of up to four particles; limited by the fact that an actuator must be on each corner of DM area projected onto an individual trap forming lens for *x y* control plus one actuator in the centre for *z* control, while also correcting for beam errors caused by drift of the optical

elements. The controller is a software routine, written in Matlab, running on a standard PC. The beam sensing element is a grid of micro lenses called a lenslet array (LA), which samples the beam at each lens location. This type of sensor is called a Shack-Hartmann type wavefront sensor (SH-WFS, simply WFS here), it will be described in more detail later in this thesis. At the controller's clock rate, the WFS senses the beam quality after the light has hit the deformable mirror, and the computer uses these measurements to make adjustments to the deformable mirror's shape to maintain an ideal beam. Because the sensor makes measurements after the beam is partially corrected by the deformable mirror, it only senses residual error, and makes incremental adjustments. In control terminology this is called closed-loop control.

The utilization of a closed-loop AO system, using a DM and SH-WFS, for an optical tweezer is a new development. Other optical trapping systems have used two methods for manipulating optical traps:

1. Beam steering → Acousto-optic deflectors (AOD's)[19], galvo mirrors [20]
2. Phase change → Spatial light modulator[21][22], digital micromirror device (DMD)

These devices have only been "adaptive" in their ability to sense and eliminate drift in trap location, caused by small movements of the optical elements, by manipulating the beam with a phase shape called tip/tilt. Static aberration correction has been achieved using SLM's. In this experiment, the DM-WFS AO system is able to correct in closed-loop for tip/tilt, along with many other optical aberrations caused by drifting optics and

misalignment. Control over higher order aberrations has a great impact on the trapping behaviour for particles much smaller than the laser wavelength [23][24][25][26]. At these sizes the diffraction pattern of the laser focus determines the trap stiffness. Aberrations tend to spread out the laser intensity, decreasing trap stiffness. Some aberrations result in non-symetrical diffraction patterns, causing an asymmetry in the stiffness value. This adds error to the use of the tweezer as a force probe if unaccounted for, or can be purposefully exploited [12]. By manipulating aberrations in closed loop, researchers can reproduce aberration conditions, increasing experimental repeatability and comparability to other research. Additionally, the system is able to manipulate the trap position in three dimensions.

Basic method of Optical Trapping

Being able to hold objects with a beam of light is not something people, the author included, experience in day to day life. Supervisors might wish they could keep grad students in their chairs by simply shining a flashlight on them, however this is not to be. Optical trapping requires a great number of particular conditions in order to occur; however, upon understanding these conditions, optical trapping is not particularly difficult to achieve experimentally.

An object is trapped when it is subjected to opposing optical forces, of comparable scale, such that an equilibrium position is reached. Any small movement from the equilibrium will subject the particle to a restoring force, pushing the particle back into the trap. Effectively, the particle is tethered by a spring to its rest position. Depending on the size

of the particle with respect to the wavelength, different physical processes cause trapping to occur [24]. These are outlined in Table 1.

Particle Diameter *d* versus wavelength λ	Trapping Model	Working Principle
$d < \lambda/10$	Rayleigh [1]	Polarization of the particle in the presence of a non-uniform electromagnetic field
$0.5\,\lambda < d < <\lambda$	(none) [27]	Combination of polarization and ray optics
$\lambda < < d$	Ray Optics [28]	Conservation of momentum, Fresnel equations

Table 1 - Models used to describe optical trapping

In this experiment, the trapped particles are approximately 10 times larger than the wavelength, and trap stiffness should be well predicted using ray optics [28]. According to the ray optics model, along the beam axis the opposing forces of light are those due to scattering, which tend to push the particle down the beam by photon pressure, and gradient forces due to refraction which tend to oppose scattering. Radially, the scattering force tends to push the particle out of the beam, however for particles suitable for trapping it is overwhelmed by the gradient force which acts towards the beam centre[28].

There are three basic types of apparatus that use optical forces to trap particles, depicted in Figure 3.

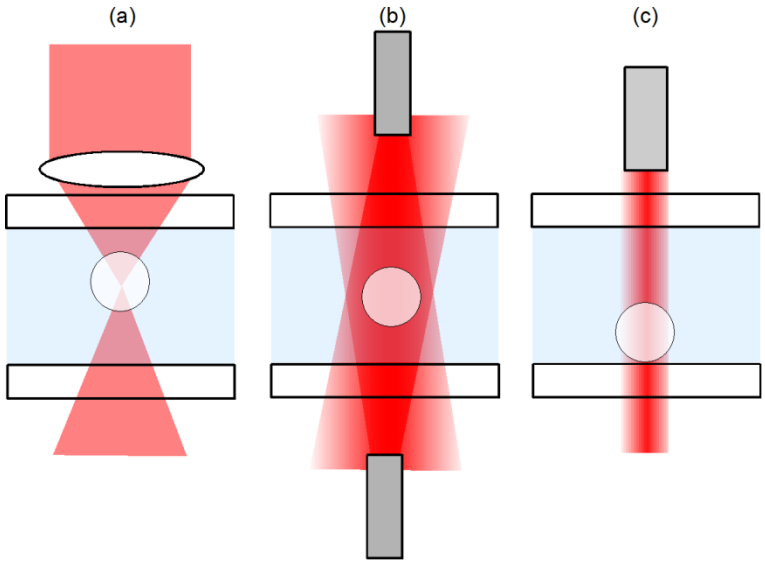

Figure 3 - Three common setups to achieve optical trapping. From left: Optical tweezer using a lens with a high angle of convergence (numerical aperture), a two-beam setup commonly created from two fibre optics, and a single collimated beam trap using a fixed surface. In all cases, the trapped particle is depicted in water between two glass microscope slides.

A brief description of the working method of each will now be given. The simplest method employs a microscope slide as a rigid surface against which to push the particle against using laser light, Figure 3c. In Figure 3b two diverging beams are directed at each other and the intensity gradient is sufficient to hold the bead radially. The restoring force, along the direction of beam propagation, is replaced by the scattering force of the second beam. These setups were first used in 1970 by Arthur Ashkin [4], [29]. Figure 3a shows an optical tweezer, which uses a single beam which is converging steeply to a focus. The rapidly decreasing intensity past the focus decreases the scattering force, while refraction of the light rays creates a restoring force pushing the particle back towards the focus. Along with the relatively large 10um particles trapped here, particles down to several

hundred nanometres in size can be trapped in an optical tweezer. In this latter case trapping is governed using the Rayleigh model, Table 1. In the Rayleigh regime, particles become polarized in the non-uniform electro-magnetic field caused by the converging light beam, resulting in a net force towards the focus; along the steepest intensity gradient.

In this work, a very high angle of convergence lens is used to create the steep intensity gradient along the optical axis required to stably trap particles in an optical tweezer. A lens's angle of convergence is typically given in terms of numerical aperture, defined in Figure 4.

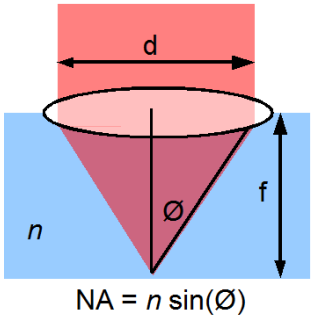

Figure 4 - Optical tweezers rely on a highly convergent laser beam to create the necessary gradient forces. Convergence is typically given in terms of numerical aperture (NA), which is related to the index of refraction in the medium, n, and the ratio of beam diameter, d, to focal length, f.

Numerical aperture (NA) for an optical tweezer system typically ranges between 0.85 and 1.3. From the definition of numerical aperture, Figure 4, a NA above 1 is only possible when the index of refraction exceeds 1. Air only has an index of refraction of 1, so a high-NA optic is typically immersed in a fluid such as oil or water, which have a higher

refractive index. Water immersion is convenient for biological specimens which tend to be prepared in water, having a refractive index of 1.3. Microscope objectives, the optic held close to the sample by a microscope, have been developed with NA's as high as 1.65 (Olympus APO 100x) although 1.35 is more commonly the maximum. Microscope objectives are the most common focusing optic used in optical tweezers because they have the required NA, and can also be used to image the trapped particle. Objective-less tweezers have been demonstrated by [30] where a single-mode fiber optic was shaped at one end to form a basic lens. Blu-Ray optical disk readers have an optic with a numerical aperture of 0.85, only 0.05 less than that used in this experiment. It would be interesting if this low-cost item could be used to form an optical tweezer.

Trapping Forces – Conservation of Momentum

As discussed, an optical tweezer is able to hold a cell or small particle using a beam of laser light coming to a focus with a large convergence angle (numerical aperture).For particles much larger than the wavelength (*$d > 6\lambda$ @ λ=1064nm*[28]*)*, a good model of optical tweezers can be derived from the conservation of momentum and a ray trace diagram. Because light has momentum, an angular change in ray direction causes a change in momentum resulting in the application of a force on the particle. The greatest possible angular change occurs when the ray is incident normal to the surface of an object. If the object is an ideal mirror, reflecting all incident optical power, the force given by the rate of change of momentum is given by the following expression [13].

$$F = \frac{2P}{c} \qquad (1)$$

Where P is the optical power, typically in the order of tens of milliwatts for optical tweezers, and c is the speed of light. This results in optical forces in the order of piconewtons (1E-12 N), which is approximately an order of magnitude larger than the force due to gravity for particles with a diameter of 10um.

Optical trapping, in the ray optics regime, can be described using a ray-trace diagram of the laser and trapped particle, and computing the force due to changes in ray direction as governed by the laws of reflection and refraction. Utilizing the Fresnel equations [31], the energy of the ray is divided between these secondary rays depending on the relative refractive index of the particle and surrounding medium, and the ray's angle of incidence with respect to the particle's surface. For particles that are good candidates for trapping, the amount of reflected light is much smaller than the refracted portion [24].

Given that photons tend to push the particle down the beam, the gradient force opposing this push is the least intuitive force to understand. In Figure 5, a particle is shown a distance ***d*** down-beam from the natural focus of the optical tweezer. The figure is a highly simplified version of the true system, neglecting all but two rays, but it gives valuable insight.

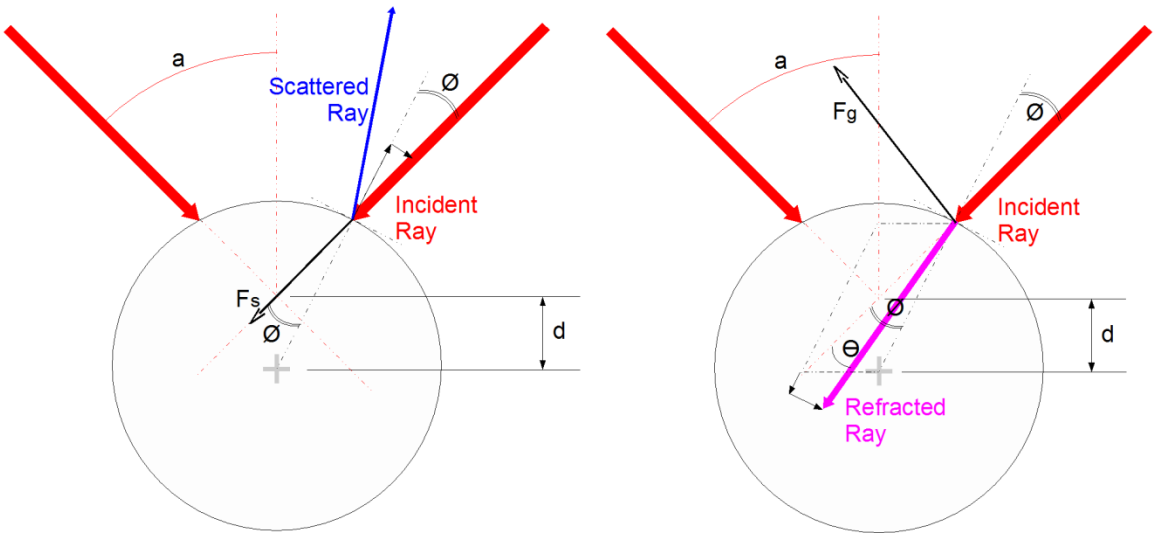

Figure 5 - Ray optics can be used to describe how an optical tweezer traps particles in a stable position if the particles' dimensions are much larger than the wavelength. The figure depicts the case where the bead is centered on the beam axis and the focus is some distance *d* from the bead center. The left and right image show how an incident ray (red) causes a scattering force *Fs* and gradient force *Fg* due to the resulting scattered and refracted rays. When the bead is centered, as depicted, it is clear that the sum of the radial components of *Fg* and *Fs* cancel when the contribution of each ray given distance from the bead center is accounted for. What remains are apposing contributions along the optical axis due to *Fs* and *Fg*.

Two highly converging rays are incident on the trapped particle, each resulting in two secondary rays due to scattering and refraction. The scattered ray creates the force due to photon pressure, tending to push the particle farther down beam. The refracted ray is responsible for the gradient force which tends to pull the particle up the beam until ***d*** is approximately zero[28]. In both cases, summation of all the radial components of force cancel with the contribution of all rays around the spherical particle.

The direction of the gradient force, ***Fg,*** is not intuitive but can be understood using an example. Imagine a person standing inside the trapped particle, upside down, with their

feet at the point where the ray intersects the particle, Figure 6. The person is shown bending a refracted ray back towards the surface normal, resulting in reaction forces pushing his feet against the particle boundary. This represents how the particle experiences force due to the change in ray direction.

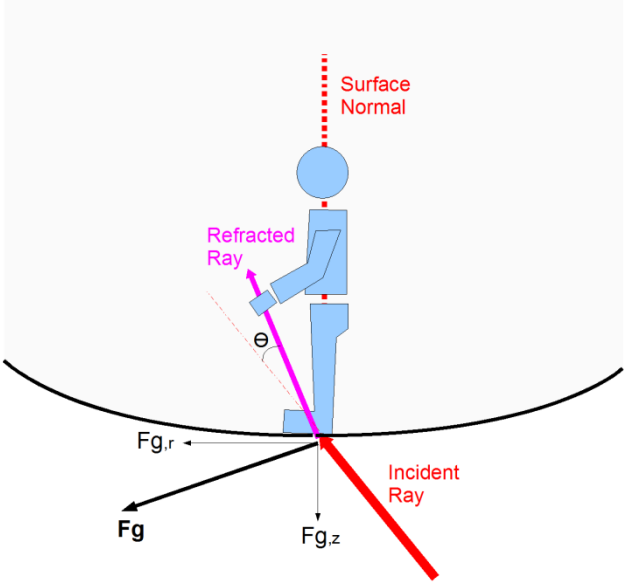

Figure 6 - Cartoon depicting the direction of the gradient force due to refraction of the incident ray. The person is depicted, standing inside the trapped particle, pulling the refracted ray back from its nominal direction (dotted purple) by the angle θ. The reaction forces applied to the bead are shown at their feet. The depicted direction of angular change, and Fg,z , require the particle to have a greater index of refraction than the surrounding medium.

With no difference in refractive index between the particle and surrounding medium, the ray would travel straight along the dotted red line in Figure 5. However, because the index of refraction of the particle is greater than the surrounding medium, the ray is pivoted up by the particle towards the surface normal. This causes a reaction force in opposition to the direction of beam propagation, as well as a radial force towards the beam centre. As predicted by the above model, it has been shown [4] that for particles,

(air bubbles, n=1), with a lower refractive index than the surrounding medium, (water, n=1.33), the direction of the reaction force reverses and acts along the direction of beam propagation adding to the scattering force. Ashkin performed a complete ray trace analysis of an optical tweezer and found that the overall force vector is maximum when **d** is slightly less than the particle radius, and points towards the focus[28]. Also, the ray trace diagram shows that as NA becomes small, scattering forces dominate and trapping is lost. Ashkin also showed that if the particle's refractive index is much larger than the medium, scattering forces dominate because too large a percentage of energy is reflected, as predicted by the Fresnel equations.

Similarly, a ray diagram can be used to show how a particle in an optical tweezer, radially offset from the beam centre, is drawn back to the centre of the beam (Figure 7).

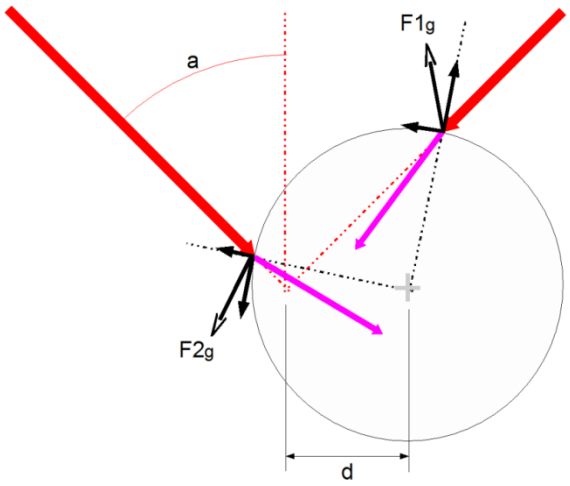

Figure 7 - Ray diagram showing two highly converging rays incident on a trapped particle that is offset radialy from the beam centre by a distance, d. The gradient forces are shown, scattering forces have not been depicted and are small in comparison[28]. The components of F1g and F2g along the axis of beam propagation appose, whereas the radial components add, drawing the particle towards the laser focus.

In the highly simplified drawing, two convergent rays symmetric with the optical axis are shown. In this drawing, only refracted rays are shown for simplicity. While the rays strike the particle at different angles of incidence, they are both refracted towards the surface normal. This causes reaction forces that generally oppose each other along the beam axis, and sum radially, causing the particle to be drawn towards the centre of the beam.

Wavefront and Optical Propagation

A basic description of the wave nature of light is given here to provide background on the method used for manipulating the position of the trapped particle. A wave description also provides insight on other critical phenomena; such as: beam aberration, and wavefront. The theory presented here is brief and not rigorous in the mathematical sense. For more detail a good text is Roddier et. al. [32]. The propagation of a wave *U* along the beam axis *z* is described by the Helmholtz wave equation (2).

$$U(x,y) = A(x,y)exp\big(i\zeta(x,y)\big) \qquad (2)$$

The wave consists of two components, the real component A and an imaginary component expressed in complex exponential form. The real component, A, is the amplitude of the light wave's electric field. The complex exponential, variable ζ, represents the phase of the field. The components *x*, *y*, and *z* in this report are defined as follows

- *z* the direction of beam propagation in the absence of distortion
- *y* the direction opposing gravity
- *x* perpendicular to *z* and *y*, to the right when looking up *z*

Notice that there is no *z* term in the Helmholtz equation; this is because the equation is valid only at planes along the optical path with the same wavefront, *U(x,y)*. This is a critical point, relating to how optical elements are placed on the experimental bench. Because the deformable mirror, wavefront sensor, and microscope back aperture must all work together, they must be placed in planes with identical wavefront. These are termed conjugate planes, and because they have the same wavefront they are described by the Helm-holtz equation.

The portion of the equation that is measured and controlled by the AO system is the complex exponential term $\zeta(x,y)$, the wavefront's phase, and is given in terms of radians. For simplicity, the wavefront phase will be referred to simply as the wavefront because it is the only portion controlled by the system. The wavefront can be conceptualized using a ray-trace diagram depicting optical-path length. A depiction is given below in Figure 8.

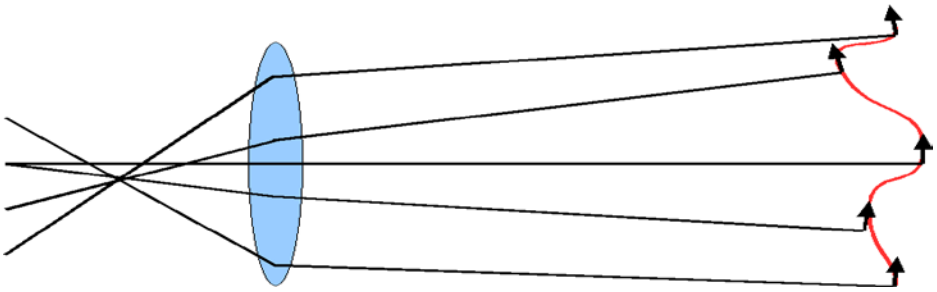

Figure 8 - Wavefront phase can be depicted as the optical path length of the collection of rays forming a laser beam. The figure shows five rays which have been frozen some time after emission from the laser. Due to aberrations such as misalignments, some rays have travelled farther than others. Tracing a line perpendicular to each ray gives an image of the 2-D wavefront.

If the ray trace is frozen after a given time of flight, all rays would ideally have traveled the same optical-path length. However, due to imperfect optics or non-flat shapes placed on the deformable mirror, some rays will have travelled farther than others. The wavefront can be visualized as a line drawn connecting the heads of these frozen rays, where the line intersects each ray perpendicular to its direction of propagation.

Using the ray description of wavefront shown in Figure 8, it's obvious the wavefront does not remain constant through the beampath because rays will constantly be moving towards or away from each other. This causes the light to change in phase and amplitude as it travels. However, when the laser is transformed through a lens pair separated by the sum of their focal lengths, the phase and amplitude at a plane before the lenses will be duplicated after the lenses. These are the conjugate planes. By placing the deformable mirror in a conjugate plane with the back aperture of the lenslet array and trapping objective, the devices all share the same wavefront.

The principle of conjugate planes is key to the working method of this experiment so an example is given below in Figure 9. The plane of the DM, P1, and the back aperture of the objective, P2, are shown, the plane of the lenslet array has been left out for simplicity.

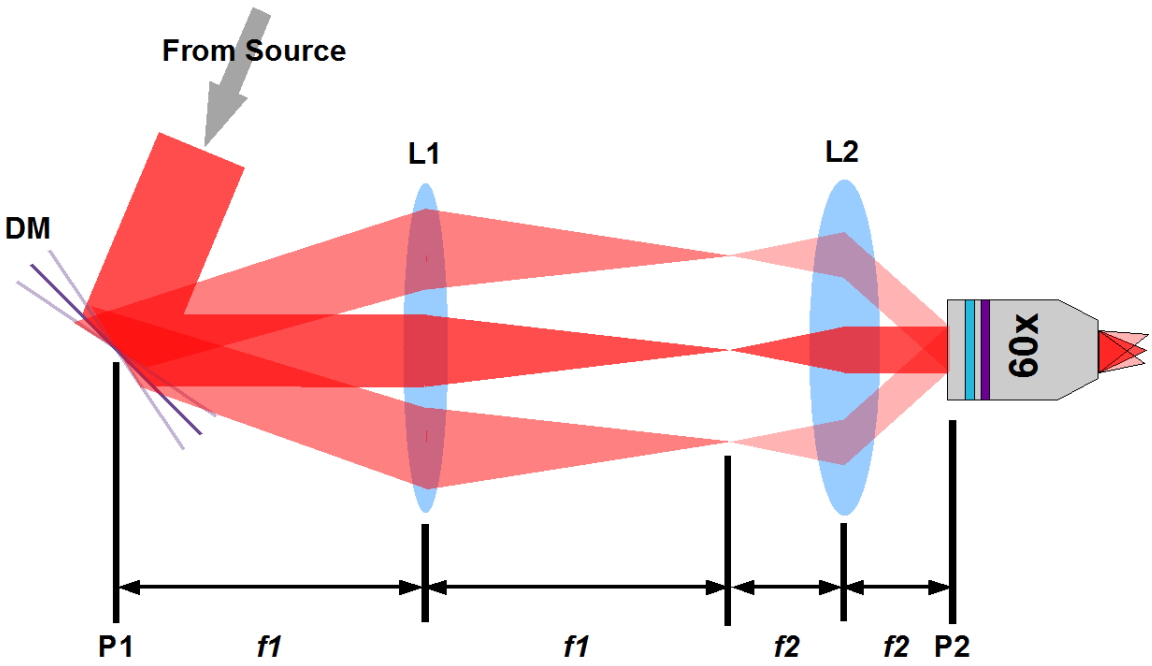

Figure 9 - Placement of the deformable mirror, microscope objective, and relay lenses' (L1 & L2) are critical in order to control trap position. By locating the deformable mirror and objective one focal length past the telescope, the wavefront at the DM is reproduced at the back aperture of the objective. Using this setup, the planes P1 and P2 are said to be conjugate.

As discussed above, rays at conjugate planes share the same wavefront. Therefore, if a mirror is placed in one conjugate plane, wavefront tilts of the mirror are duplicated in the other plane. As shown in Figure 9, although tilting the mirror changes the optical path, tilts do not cause the beam to change location on the back aperture of the objective because they are in conjugate planes. Also, tilting the mirror causes a shift in the objective's focal position. This is the mechanism used to manipulate the trap position in the *x,y* plane. Looking closely at Figure 9, the DM tilt at plane P1 is actually reversed at plane P2. This is because the lens telescope L1 and L2 reverses the image. Also, the angle of the wavefront tilt scales with the ratio of *f1/f2*. This is important because the

magnitude of trap displacement scales with the angle of the wavefront tilt at the back aperture of the microscope objective. Practically, this means that if two DM's can create tilt's with equal angular change, a larger diameter DM will produce larger trap displacements.

Describing Wavefront using Zernike Modes

The wavefront, which was defined as an optical plane of deviations from a nominal optical path length, is often described as a sum Zernike modes. Zernike modes are a set of polynomials that are orthogonal on a unit disk (useful given the circular beam shape in most optical systems). Because the modes are orthogonal, a given wavefront can be modeled by the sum of a series of Zernike polynomials, each multiplied by a particular constant.

Zernike polynomials are also well suited for describing optical wavefronts because the lower order polynomials represent very common wavefront errors such as: tip, tilt, defocus, astigmatism, spherical aberration and coma.

The definition of Zernike polynomials is given for reference in (3) and (4).

$$Z_n^m(\rho,\theta) = N_n^m R_n^{|m|}(\rho)\cos(m\theta) \qquad (3)$$

For: $m \geq 0$, $0 \leq \rho \leq 1$, $0 \leq \theta \leq 2\pi$, and

$$Z_n^m(\rho,\theta) = -N_n^m R_n^{|m|}(\rho)\sin(m\theta) \qquad (4)$$

For: $m < 0$, $0 \leq \rho \leq 1$, $0 \leq \theta \leq 2\pi$

Where N_n^m is the normalization factor in (5).

$$N_n^m = \sqrt{\frac{2(n+1)}{1+\delta_{m0}}} \qquad (5)$$

Where δ_{m0}= 1 if *m*=0, otherwise δ_{m0}= 0. And where $R_n^{|m|}(\rho)$ is the radial polynomial (6).

$$R_n^{|m|}(\rho) = \sum_{s=0}^{(n-|m|)/2} \frac{(-1)^s (n-s)!}{s![0.5(n+|m|)-s]![0.5(n-|m|)-s]!} \rho^{n-2s} \qquad (6)$$

The complete set of Zernike modes is infinite, however the vast majority of wavefront error (aberration) practically encountered can be described using the first 20 or so modes. Also, as the polynomial order increases, so does the spatial frequency of wavefront error. Therefore, the order of Zernike modes that can be corrected for by a given DM increases with the number of DM actuators. The first 21 modes, illustrated in Figure 10, should be well corrected by the 52 actuator DM used here.

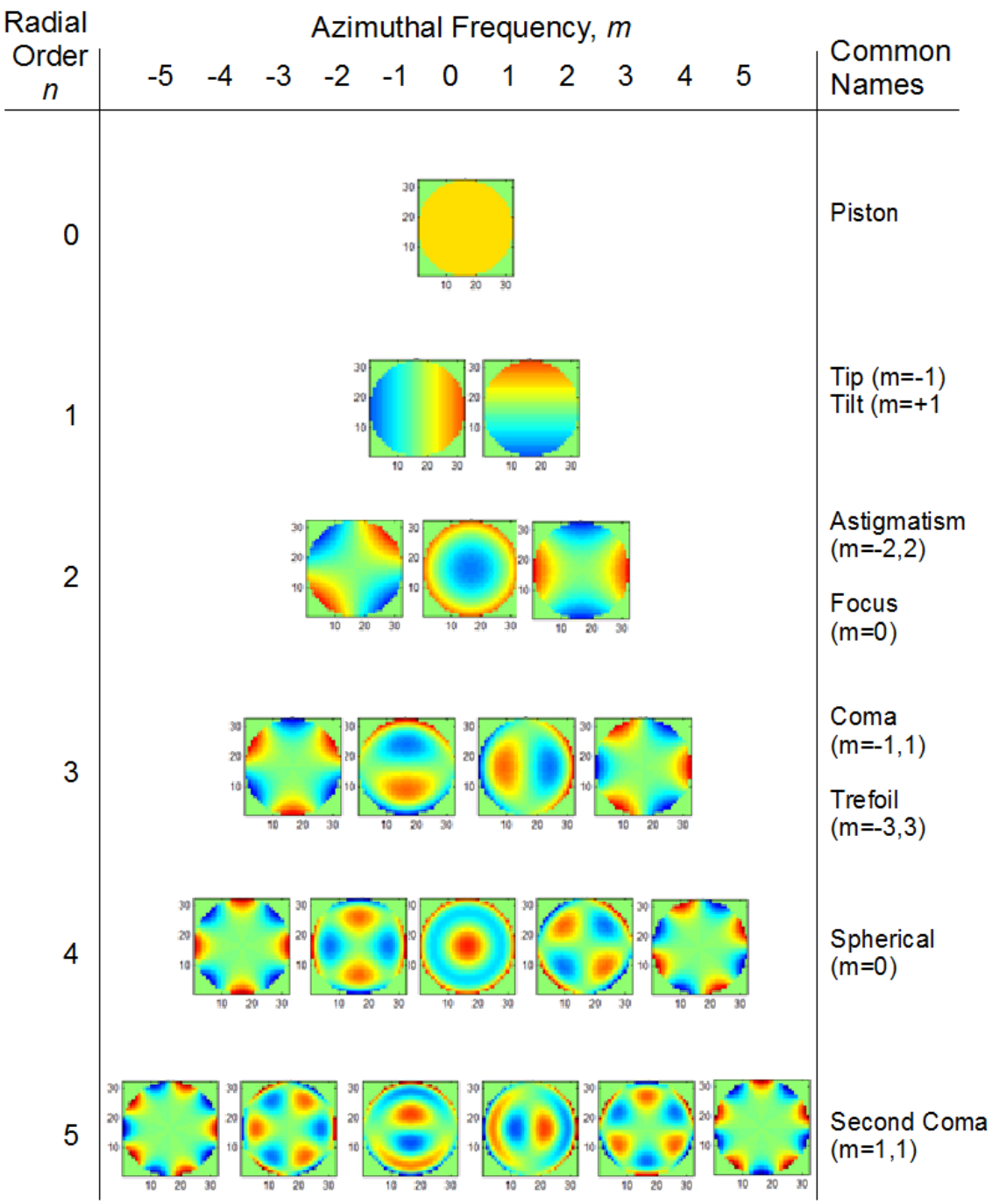

Figure 10 - Diagram of the first 21 Zernike modes. Wavefront shapes are often expressed as a sum of Zernike modes of various magnitudes.

The radial order *n* and azmuthal frequency *m*, refer the definition of the Zernike polynomials given above.

Using a Deformable mirror to Correct for Wavefront aberrations

Deformable mirrors have been developed for several different applications such as: astronomy, free-space optical communication, laser induced fusion, and observation of earth orbiting satellites. Several commercially available deformable mirrors are shown in Figure 11.

Figure 11 - Three types of deformable mirrors. From left to right: a high-speed low-stroke MEMS DM (Boston Micromachines), a large-stroke mid-speed magnetic DM (ALPAO), a large stroke piezo DM designed for high-power applications (Xinetics)

The working principle of a deformable mirror used for correcting wavefront aberrations can be explained using the optical path length description of a wavefront shown in Figure 8. The deformable mirror is commanded by the control computer to take a shape that equalizes the path length of all rays; by shortening the path for some, while lengthening it for others, thus achieving a flat wavefront. The required displacement is simply one half

the difference in path length, as the beam travels to the DM surface back again to rejoin the other rays, Figure 12.

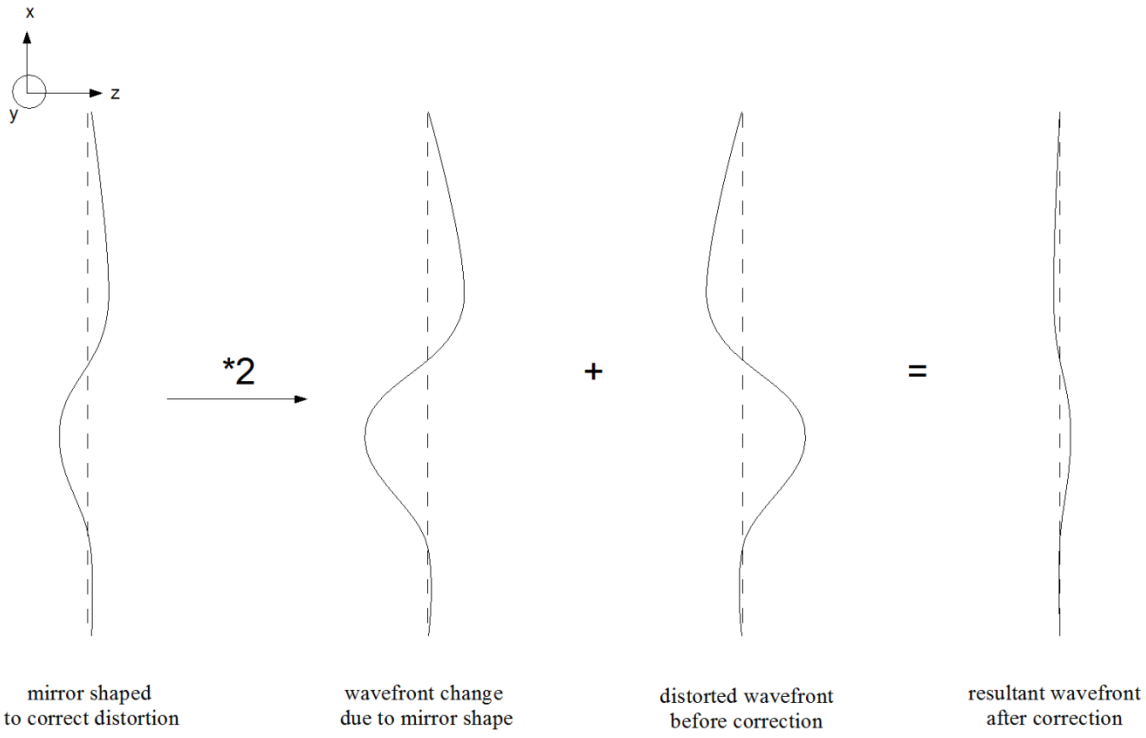

Figure 12 - Errors in the wavefront can be corrected for by reshaping the DM. The figure shows the relationship between wavefront and DM shape to correct for wavefront error.

Alternatively, the control computer can command the DM to purposefully add useful wavefront aberrations. For instance tip and tilt Zernike modes control trap position in *x* and *y*, and the defocus mode controls position in *z*. After the wavefront is focused by the trapping optic, the effect of these modes remain independent, meaning *x*,*y*,*z* trap position can be controlled by summing tip, tilt and focus modes. By dividing the DM area into sections, and placing a grid of lenses in a conjugate plane, the DM can individually control the position of multiple traps.

Principle of Operation of a Shack-Hartmann Wavefront Sensor

The wavefront sensor (WFS) combines an optical element called a lenslet array, a CCD camera, and software. The lenslet array is a rectangular grid of mold-formed lenses. The lenses are formed on a plastic substrate several hundred microns thick, which is bonded onto an optically flat glass window. An example of the type of lenslet array used in this experiment is given in Figure 13.

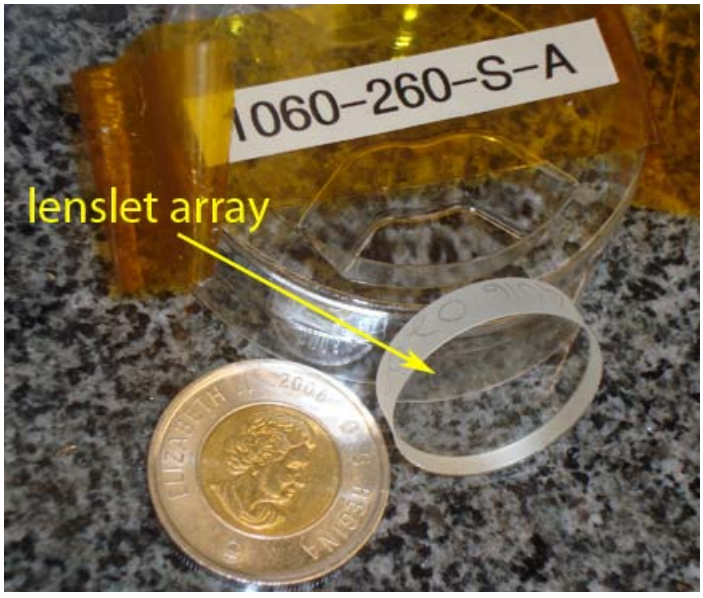

Figure 13 - A photo of the wavefront sensor's lenslet array, similar to the one used in this experiment. A toonie is included for scale. The individual micro-lenses (lenslets) are not apparent in the photo.

The lenslet grid fills the entire diameter of the optical flat, the tweezer's small beam uses only a small portion of the available lenslets. The sensor is called a Shack-Hartmann type wavefront sensor (SH-WFS). As discussed earlier, the lenslet array must be placed in a conjugate plane with the microscope back aperture, and DM, to give accurate readings.

The purpose of the wavefront sensor is to determine the wavefront at the back aperture of the trap forming microscope objective. It does this indirectly by dividing the beam with a grid of lenses, each forming a focus on the CCD camera. The average wavefront slope (tip/tilt) offsets each lenslet focus from its central position, proportionally to the slope of the wavefront across its aperture. A pictorial representation of a single row of lenslets is given in Figure 14 (a). The figure shows a distorted wavefront striking a row of lenslets, causing a shift in focus. The image in (a) is rotated in Figure 14 (b), this time four lenslets of the grid are shown. An equation relating focus shift to average slope is also given.

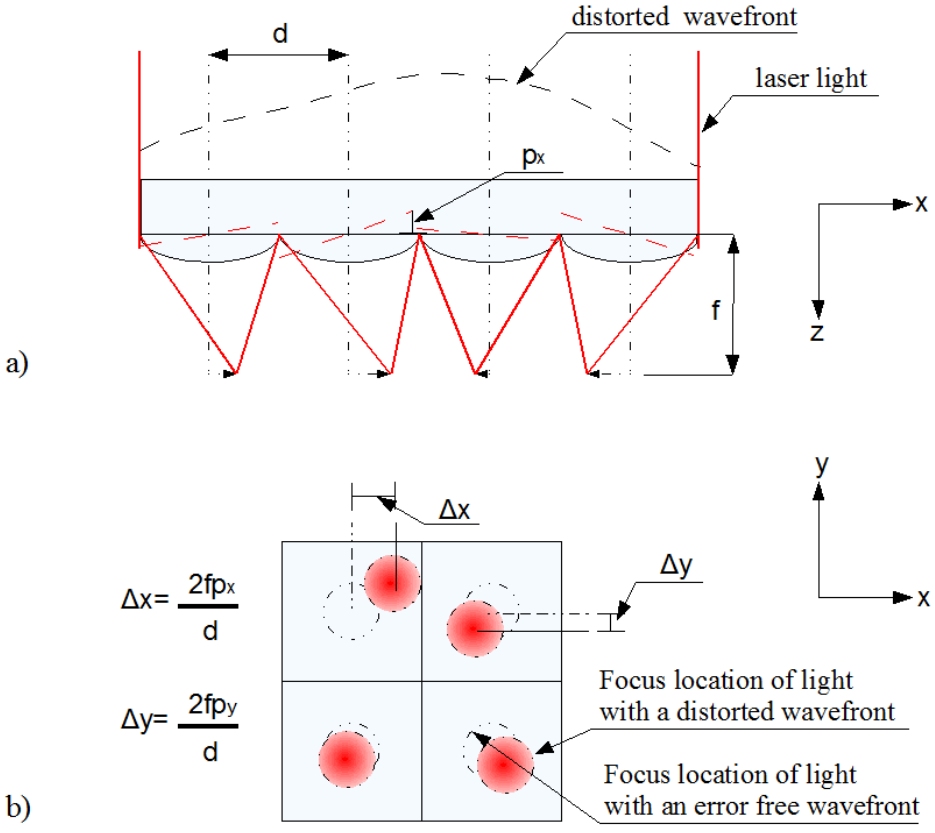

Figure 14 – Micro-lenses in the wavefront sensor's lenslet array, called lenslets, produce a focus that is displaced in *x* and *y* according to the average tip/tilt of the wavefront entering the lenslet

The ratio of distortion *p* and lenslet diameter *d* in the focus-shift calculations, shown in Figure 14 (b), show distortion is related to wavefront slope. Since focus shifts are proportional to wavefront slopes, the SH-WFS is a gradient sensor. The overall wavefront can be reconstructed by integrating the slope measurements across the *x y* plane of the beam, with accuracy depending on the number of lenslets that sample the beam.

Each lenslet's shift in focus is determined by calculating the centroid of the image of the focus recorded by the wavefront sensor CCD camera. This gives the measurements of focal positions with sub-pixel accuracy. The centroid is calculated in the *x* and *y* directions, for N lenslets, there are 2*N measurements. Control stability requires that there be at least as many lenslet measurements as deformable mirror actuators. A screen shot showing the CCD image of the lenslet array focuses is given in Figure 15.

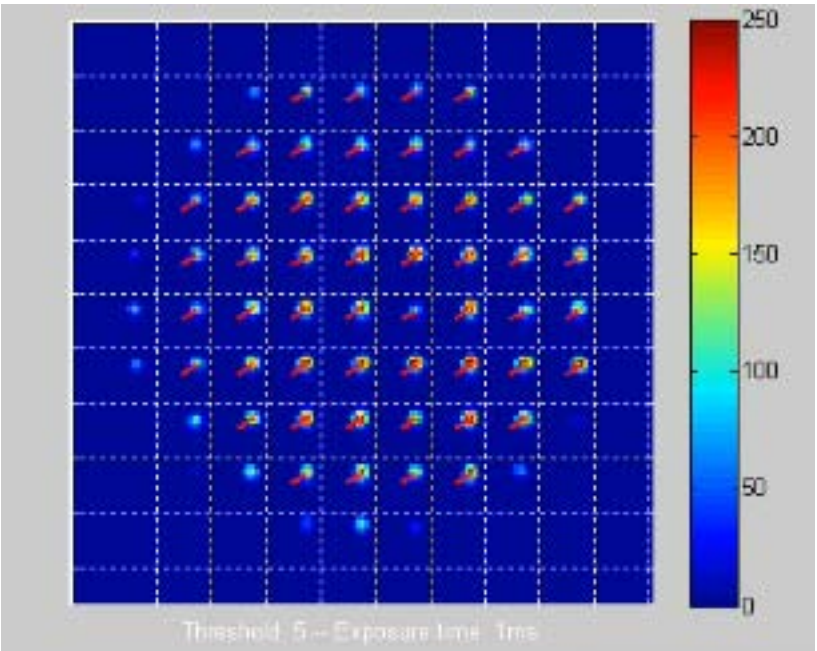

Figure 15 - This image is formed by the wavefront sensor CCD camera. Each lenslet focus is displaced in *x* and *y* by the same amount (red lines), indicating a global tip and tilt in the wavefront.

The figure shows the lenslet focus are offset in *x* and *y* by the same amount for each lenslet, indicating the presence of equal wavefront slope on each lenslet. This corresponds to wavefront having a global tip and tilt, as is used to move the trap in *x* and *y*.

Describing the Operation of a Simple AO System

The adaptive optics system consists of the sensing element, actuator, and control software. This section will detail the working principle, and hardware layout of a basic adaptive optics system. The actual hardware used is given in Chapter 2, and the control

system implementation will be given in Chapter 3. A basic schematic below shows how an adaptive optic system works to correct for wavefront errors.

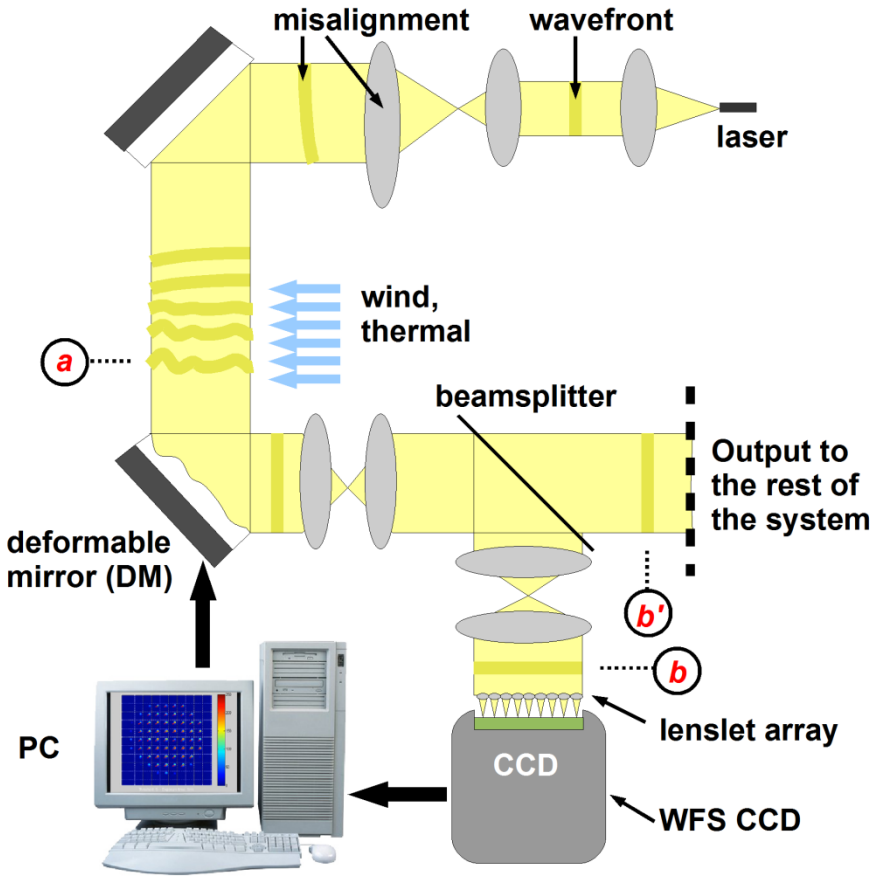

Figure 16 - Basic adaptive optic system. The phase plane, or wavefront, of the laser is given in darker yellow. It becomes progressively less flat due to misalignments, vibrations, thermal expansion, and fluctuations in air pressure. The phase plane is sampled by the lenslet array, after partial/full correction by the deformable mirror.

Looking in detail at the system, the controller takes measurements of the wavefront at the lenslet array, and makes adjustments to the deformable mirror. In Table 2 the wavefront is shown for several controller steps with respect to the following planes, depicted in Figure 16: plane *a* before the deformable mirror; conjugate planes *b* and *b'* at the lenslet

array and the system output. Also given in the table are the DM shape, and wavefront sensor measurements made by the lenslet array.

AO System Position	Wavefront at controller step #:			
	1	2	3	4
a			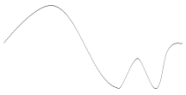	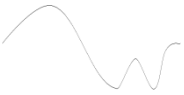
DM				
b & b'				
PC	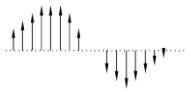			

Table 2 - Wavefronts before the DM and afterwards, *a* and *b&b'* , are shown after the controller acts on the DM at successive controller iterations. The arrows in the PC measurement represent the discrete measurements made by the lenslet array. Only one dimension of the wavefront is shown, in reality the system acts in 2D. The controller works to flatten the wavefront.

Some error exists in step 1 and is corrected in step 2. In step 3 more error is added and corrected in step 4. The closed-loop nature of the controller is shown in steps 3 and 4, where the sensor measurements only show the additional error because the DM in step 2 has corrected for the original error from step 1.

In reference to the description given above, the wavefront sensor is composed of the lenslet array and CCD, and the controlled actuator is the deformable mirror. The phase of

the laser at the back aperture of the trapping optic, $\zeta(\mathrm{xi}, \mathrm{yi})$, is related to the shape of the deformable mirror, $s(xi, yi)$, through a very simple relationship, given below in (7).

$$\zeta(\mathrm{xi}, \mathrm{yi}) = -2s(xi, yi) + \sum \emptyset(xi, yi) \qquad (7)$$

Where $\sum \emptyset(xi, yi)$ is the sum of all the phase aberrations between the laser source and the WFS. The multiple of two between deformable mirror and phase shape is due to the fact the light must "swim out and back" to the deformable mirror position. Note that the adaptive optic system is susceptible to "false aberrations" between the beam splitter and wavefront sensor. This is commonly referred to as non-common path error. To address this, special care must be taken to align and select the optics used after the beam splitter.

Chapter 2 – Experimental Apparatus

The optical tweezer apparatus combines elements for beam sizing, a brightfield microscope, an adaptive optic system, a trapping chamber, and a flow system to calibrate the optical tweezer. A description of these elements is given in this section.

Bench Layout of the Optical Tweezer

A schematic diagram of the final bench is shown in Figure 17.

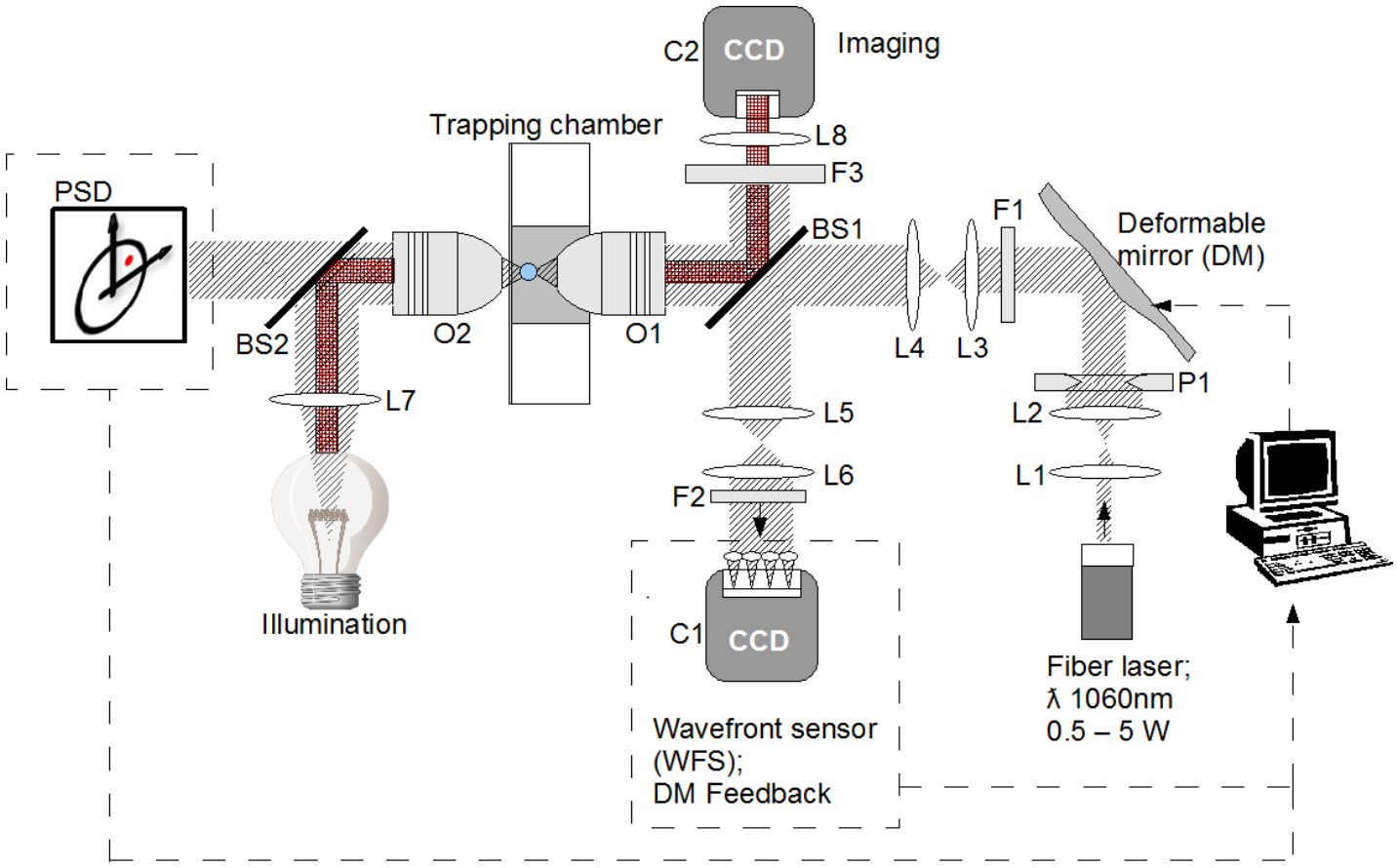

Figure 17 - Optical tweezer bench schematic. The fibre laser emits a collimated beam which is resized, and reflected off the DM, changing its wavefront. The beam is again resized to fill the back-aperture of the objective O1 which forms the trap. Part of the light is split off and sent to the wavefront sensor by BS1. Trapping light is sent through objective O2 and lands on a high-speed 2D position detector (PSD). A white light source propagates opposite to the trapping beam, producing a bright field image on the imaging CCD.

Design of the Trap Forming Optical Path

The trapping laser is 1060 nm , continuous wave (CW), fibre laser (Manlight, ML-5-CW-R-OEM-1060). The fibre laser delivers light via a single-mode fibre with a core 8 um in diameter. The core size is important because a large core, as in a multimode fibre, does not have the spatial coherence needed to create the small focus required for

trapping. The laser fibre is factory coupled to a collimating lens. The laser power is tuneable between 0.5 and 5 W, before collimation. Delivered power is lower due collimation losses, between 0.472 and 4.7 W. Power can be incremented using a hand-held controller by increments of 100mW. For more sensitive intensity control, an attenuator was used (F1, HOYA 8x ND Filter).

Trapping can be accomplished at the lowest power setting; however, the power capacity will allow future experiments with multiple trap tweezers. Feedback for maintaining constant laser power is handled internally by the laser. Alignment of the invisible laser is greatly simplified through a red pilot beam launched from the same fibre.

Light exits the laser through a collimating lens and is resized from 2.2mm to approximately 20 mm diameter with a telescope formed by a lens pair (L1 f20, L2 f350). The lens L2 is acting as a pupil, vignetting the natural 38.5 mm beam size. This was done to decrease the ratio of intensity between the centre and edges of the beam. Having a flatter intensity profile is important because the WFS CCD has a small 8 bit dynamic range. An adjustable pupil, P1, is positioned after L2 reducing the diameter to 15 mm, filling the controllable area of the deformable mirror (DM). The light is reflected from the DM into another lens pair (L3 f400, L4 f180) to resize the beam to 6.75mm such that it fills the back aperture of the trapping objective, O1.

Prior to entering the trapping objective, the laser passes through a pellicle beamsplitter (Thor labs, 92t-8r). The beamsplitter is a cellulose membrane, a few microns thick, that transmits 92% of the light, and reflects 8%. Using a pellicle, instead of a beamsplitting cube, frees up bench space, and the thin membrane eliminates ghost images. Ghost images are caused by secondary reflections in cube beamsplitters which cause error in the wavefront sensor measurements. Bench space is important because the trapping objective must be close to L4 in order to be in the conjugate plane with the deformable mirror. To provide a larger field of view in the imaging plane, the pellicle is placed at an angle less than 45 degrees with respect to the imaging plane. This increases the projected area of the pellicle and the field of view. This shallow angle could not be used with a cube beam splitter because the non-normal angle of incidence would create significant ghosting.

The laser light transmitted through beamsplitter B1 enters the back aperture of the trapping objective O1 (Olympus LUMPLFLN 60XW) and forms the steep focus required for optical trapping. The objective's numerical aperture is 0.9, and has a working distance of 2mm. This is a long working distance given the numerical aperture, 0.2 to 0.3 mm being the common range. This objective is designed to be immersed directly into water without a coverslip. The long working distance was selected to maximize the range of trap motion, and to study the effects of trapping at long distances. To a first order approximation, the relationship between a DM tilt of height p from the rest position**,** to trap displacement x is given by the equation (8).

$$x = \frac{2pf}{d} \qquad (8)$$

Where *f* is the effective focal length of the objective, and *d* is the beam diameter. Figure 18 depicts the model of the objective described by (8), where the objective is represented as a single lens.

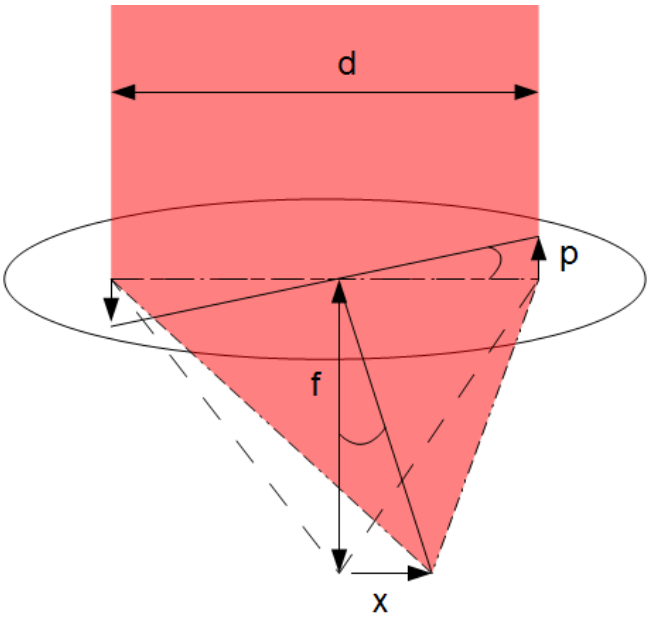

Figure 18 - A tip/tilt of the deformable mirror of wavefront amplitude p displaces the focal position by x depending on the focal length of the lens system f, and the diameter of the collimated beam d at the back aperture of the optic.

The ratio of *f/d* in equation (8) means there is a trade-off between the maximum trap displacement and minimum controllable movement. This ratio is also related to numerical aperture; a greater NA results in more precise control of trap motion over a shorter distance.

Microscope objectives are differentiated by their magnification, equation (9), which is given by the ratio of focal lengths between the image-forming lens called the “tube lens” and the effective focal length of the objective.

$$M = \frac{f_{tube}}{f} \qquad (9)$$

The effective focal length f is therefore the focal distance of the tube lens f_{tube} divided by the magnification M. In this experiment M is 60, and f_{tube} is taken as 180mm which is the industry standard. Therefore by rearranging equation (9), the effective focal length is 3mm.

When the position sensitive detector (PSD) is being used to determine trap stiffness, the trapping light from O1 is re-imaged by objective O2 (Nikon CFI-60x Achromat) onto the PSD.

Design of the Trap Imaging Microscope Path

The imaging path is used to create a bright field image of the trapping/specimen plane. The light source is a halogen lamp, which is partially collimated by the lens L7 (f150). The light hits beamsplitter BS2 (Thorlabs 92%t 8%r) where most light is discarded and the reflected portion is sent through O2 into the trapping chamber. There it is refracted by the chamber contents, and re-imaged by the trapping objective O1. In a preliminary set-up, the lamp and position sensitive device were in the opposite configuration, the lamp transmitting through the beamsplitter, however; it was found that the pellicle beamsplitter affected the PSD measurements, probably due to random fluctuations of air pressure on the beamsplitter's thin membrane. When the PSD was not in use, O2 was backed off several millimetres from the trapping plane. At this distance the rays of the white light enter the trapping plane roughly parallel with the optical axis. This greatly improved

image quality. The image transmitted by O1 is reflected by the beamsplitter BS1 and passes through F3, a low pass filter to remove reflected laser light (EO NT45-216). The image passes through lens L8 (f150) and is focussed on the imaging CCD C2 (Point Grey Research Grasshopper GRASS_5055M-C). The imaging CCD's specifications, and relation to the trapping plane, are shown in Table 3.

Pixels Width	Pixels Height	CCD Type	Max Frame Rate	Dynamic Range	Um / pixel	FOV
1600	1200	Grayscale	30 fps	8 bit (16 max)	0.119	191x140 um

Table 3- Imaging CCD specifications

Wavefront Sensor Path

The trapping laser is manipulated by the deformable mirror, resized by lenses L3 and L4, and is focused by objective O1 forming the trap. Before passing through objective O1, beamsplitter BS1 sends roughly 8% of the light onto the wavefront sensor path. The beam is resized from 6.75 mm to 1.5mm by lenses L5 (f450) and L6 (f100). The beam is divided into 52 individual beams by the lenslet array, each beam forming a focus on the CCD C1 (Dalsa CA-D1-0128A, 128x128 pixel).

Mechanical Trapping System

The mechanical trapping system is separate from the tweezer optics and has some innovative features. The role of the trapping system is to transport particles to and from the laser focus, apply external forces to a trapped particle to calibrate trap stiffness, and to position the test sample.

Trapping Chamber

The trapping chamber is an enclosure where test specimens are trapped, suspended in water, and analyzed. It contains distilled water, the particles under test, mounting provisions, and in this case a method for applying fluid flow. The trapping chamber was designed to be cleanable, and features two halves that can be separated. The upper chamber serves as a second point of support for the trapping objective, whereas in most setups the objective is supported only at the back. A model of the chamber is given in the Figure 19 and Figure 20.

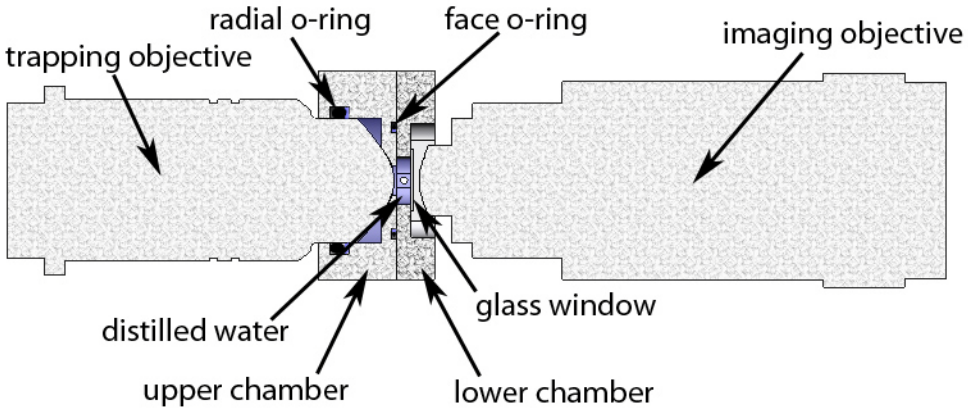

Figure 19 - Cross-sectional view of trapping chamber and objectives. Applied flow can be applied in the direction of the viewer's eye.

The trapping chamber is quite large compared to most optical traps. This allows for a more robust construction, rigid mounting, and large sample holding capability. The chamber is a custom built aluminum piece mounted to a standard 5 axis manual optics mount. The immersed objective is sealed with an o-ring and a window is cemented to the

other side of the chamber. The window is cut from a No 1.5 coverglass and allows laser light to pass through to the position sensitive detector, as well as white light for the imaging camera. The chamber's dimensions are 34x5.7x2 mm.

The trapping chamber has a port on each end allowing water to be pumped through, as shown in Figure 20.

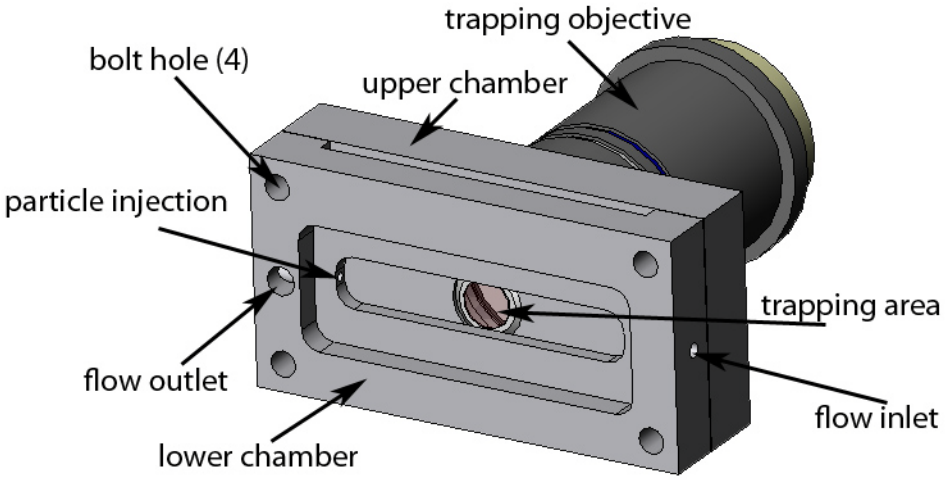

Figure 20 - 3rd Angle view of flow chamber and trapping objective. The chamber has three fluid ports; inlet, outlet, and particle injection. The seals and tubing attached to the ports, and the needle inserted for particle injection, are not shown.

The flow outlet is a hole drilled through the lower chamber, and partially through the upper chamber, bisecting a hole drilled for particle injection. Flexible Tygon tubing was glued and sealed into the holes using marine epoxy, necessary for water resistance (Lepage Marine Epoxy, 60minute). The area where the glass window is glued is several millimetres inset from the outside of the lower chamber. This extra material is necessary to achieve sufficient stiffness to effectively face seal the upper and lower chamber.

Trapping specimens are placed in the chamber via a needle passing through another port in the chamber. A more detailed drawing of the chamber is given in Appendix 1

Sample Injection

The sample is injected through a needle (Hamilton, 26s gauge, 120mm length) held by a plastic sleeve, and mounted inside an optics mount (Newport LP-1). The mount can be manipulated manually along 5 axis, shown in Figure 21.

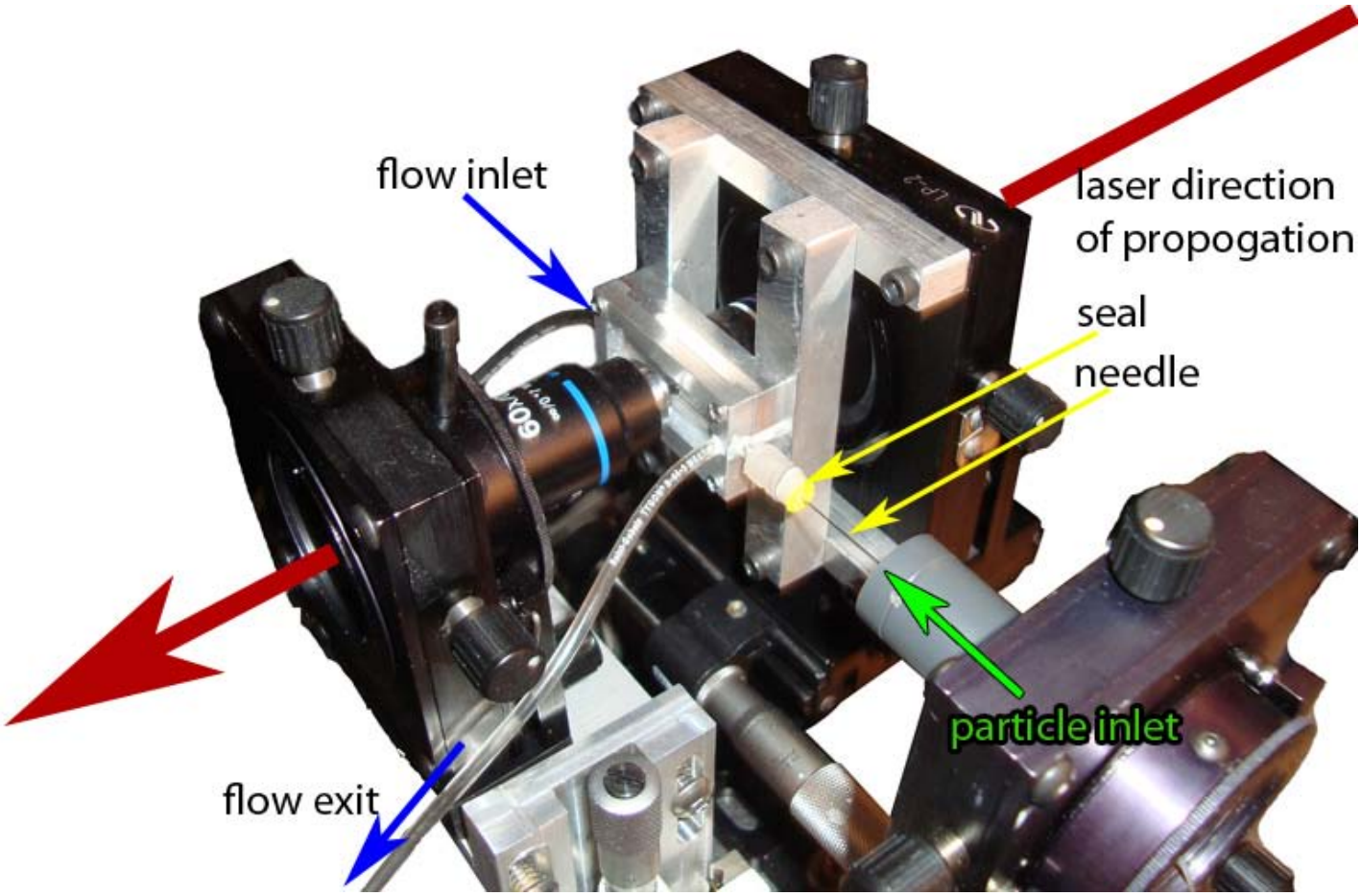

Figure 21 - Detail view of the sample injection system. Water can be pumped in through the flow inlet by manually depressing a syringe (not shown). Particles are injected through a 26s gauge needle, using another manual syringe (not shown). The trapping objective is barely visible, being hidden by the flow chamber (silver, centre of picture) and the 5-axis optical mount (black, background).

The trap chamber is sealed at the needle inlet by a rubber septum. This has been quite an effective device and after a hundred or more needle insertions it is still water tight. The needle is brought into proximity of the trap manually, observing the needle tip position via the imaging CCD. Particles are injected as a "cloud" by depressing a syringe attached to the needle through Tygon tubing (not shown). For more accurate stiffness measurements, discussed later, the chamber was first seeded with extra particles by depressing the syringe a few times before attempting to trap.

To accurately place particles into the trap, the needle bore should be no more than two or three diameters of the particle wide or particles will be wasted. Also, when excess particles are in the trapping area, a trapped particle will quickly be dislodged by another passing particle, or they may interact and become bound together. In this apparatus, the needle is long enough to pass through 20mm of the chamber, plus 20mm through the seal and tube, and tough enough to be inserted/removed from the rubber seal. This required a metal needle, preferably with a bore of approximately 20um. However, the smallest commercially available needle bore is 89um bore (needle gauge 32). A 26s gauge needle was selected because it has the bore of a 31 gauge needle (114um) with a thick wall for durability. Because the gauge is much larger than the particle diameter of interest (1 to 10um), sometimes it would dispense so many particles that trapping was difficult. A solution was found using the lab's micro elector-discharge machine (Panasonic MG-ED82W). This device resembles a 3-axis mill, however the cutting tool is an electrode

which uses electrical arcs to erode the workpiece. The device is useful for precision machining, particularly slot and hole features, in the dimensional range of 10 – 1000um. It was used to bore a small hole, perpendicular to the needle's length, near the tip of the needle (Figure 22).

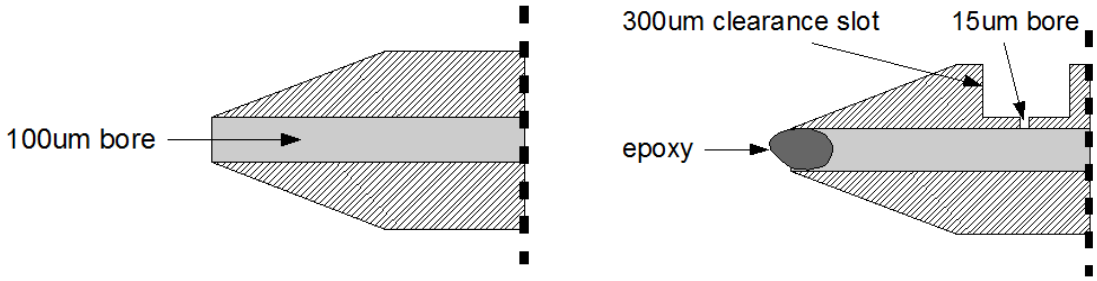

Figure 22 - The needle's bore was effectively reduced by micro-electro-discharge machining. The left image shows the convensional needle tip, and the right image shows the tip after machining. The new bore was measured to be 15um.

The re-machined needle allowed precise injection of beads into the trapping region. When the needle was correctly rotated such that the small bore was well aligned with the trap depth, each 10um bead injected could be trapped.

Pressure Pump to Generate Liquid Flow in the Trapping Chamber

The purpose of the pump is to clear the chamber of excess particles, and to generate drag forces over the trapped particle which is used to determine trap stiffness. Two pump options were tested; the first being a leadscrew-type syringe pump. However it was found that this technique required nearly a minute to start or stop the flow, due to flexibility in the syringe/plunger and the mount holding the syringe. A major improvement was made by replacing the syringe pump with a pressure pump, see Figure 23.

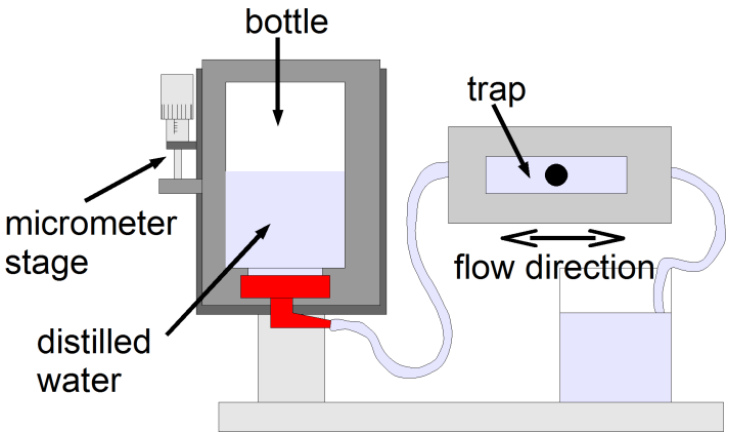

Figure 23 - Drawing of the pressure pump used to generate flow across the optical trap

The device uses gravity to pump water from a large bottle through the trap. Flow rate is adjusted by changing the height of the bottle which is mounted to a micrometer stage. Flow control is good, and can be generated forwards and backwards up to several hundred microns per second, and regulated with a precision of approximately 0.3 um/second.

Adaptive Optics System Component Parameters

The adaptive optics system consists of the lenslet array, wavefront CCD camera, and DM. The hardware has been selected such that in the future it will be able to control up to 4 traps in 3-dimensions, although this thesis details the results for only a single trap. A description of the components is given below.

Wavefront Sensor

The WFS consists of the lenslet array, CCD camera, and software. The lenslet array used here (AOA 188-8-S-A) has a focal length of 8mm, and a pitch distance between lenslets

of 0.188mm. The positioning of the lenslet array with respect to the beam is shown in Figure 24.

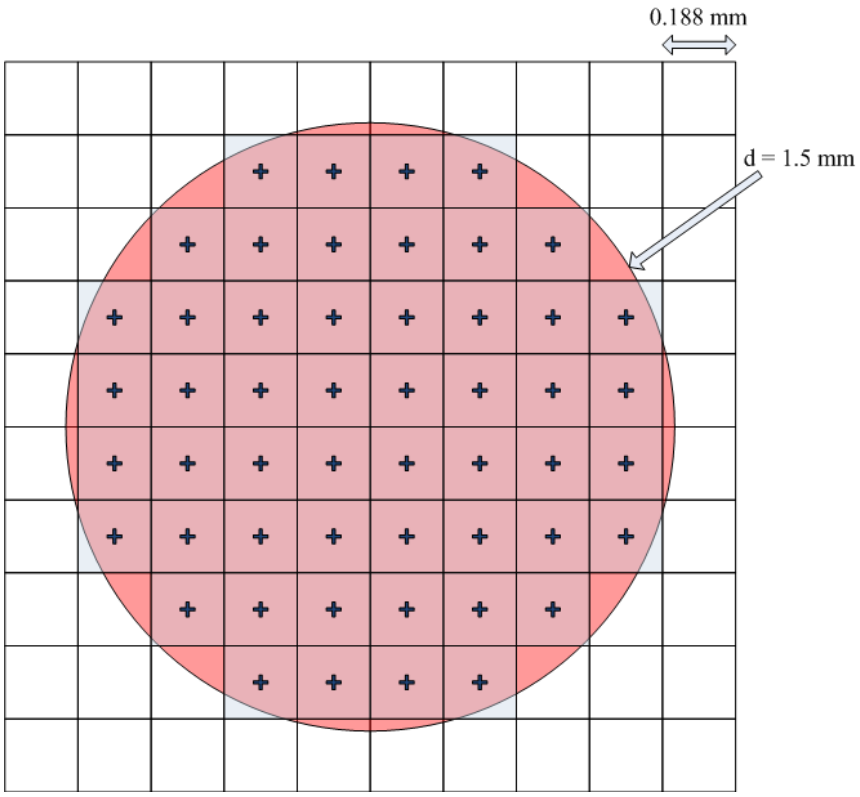

Figure 24 - Superposition of the lenslet array (grid) and the sampled beam (red). Many lenslets are not used. The data from the lenslets marked by a cross are used by the controller. Each lenslet forms a focus on a CCD, the displacement of the focus from the centre of the lenslet subaperature provides a measure of the average phase gradient across that subaperature.

The lenslet array has many more lenslets than are needed to control the 52 actuator DM. The lenslet array is positioned to equally distribute the lenslets across the beam, 8 lenslets vertically and horizontally.

The WFS CCD camera (DALSA CA-D1-0128A) is a CCD type with specifications given in Table 4.

Maximum Frame Rate (FPS)	Pixel Depth (levels)	Resolution (pixels)	Pixel Pitch (um)	Fill Factor (%)
730	256	128x128	16	100

Table 4 - Wavefront sensor CCD camera specifications

Deformable Mirror

The DM has 52 actuators on an 8x8 grid (ALPAO DM52). The main features of this deformable mirror are large stroke, zero hysteresis, and very high linearity between actuator voltage and stroke. Micro voice coils and magnets are used to manipulate the DM surface. Underneath the surface are very small permanent magnets, when current flows through a coil, the magnet above is attracted or repelled depending on the direction of current (Figure 25).

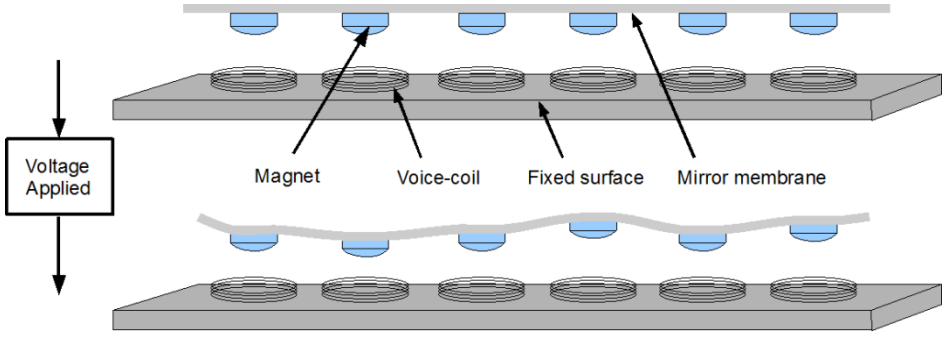

Figure 25 - The ALPAO deformable mirror uses voice coils and small magnets to deform the mirrored surface.

The mirrored surface is a flexible membrane attached to a stationary ring outside the last set of actuators. This means the edges cannot be controlled. The DM pupil is located well inside of this edge to avoid this constrained region. The mirror is shown in Figure 26.

Figure 26 - The ALPAO DM52 deformable mirror used in the optical tweezer. The mirrors 52 actuators are addressed using serial communication with between a PC DAQ card (Adlink Powerdaq 64) and DM drive electronics (ALPAO DE64).

The distance between actuator centres is 2.5mm and each actuator has a maximum stoke of 50 um peak to valley. By comparison, most deformable mirrors have a stroke of only 1 or 2 um. Practically, however, the stroke is substantially lower, depending on the desired shape, because the actuators are influenced by their neighbours as they all act on the same mirror surface. Because the deformable mirror is used to shape the wavefront of the beam, stroke is often given in terms of wavefront units, which are double the mechanical displacements because light travels "there and back" to the mirror shape. The diagram shown in Figure 27, reproduced here courtesy of ALPAO, shows the interdependence between shape and maximum stroke, given in wavefront units.

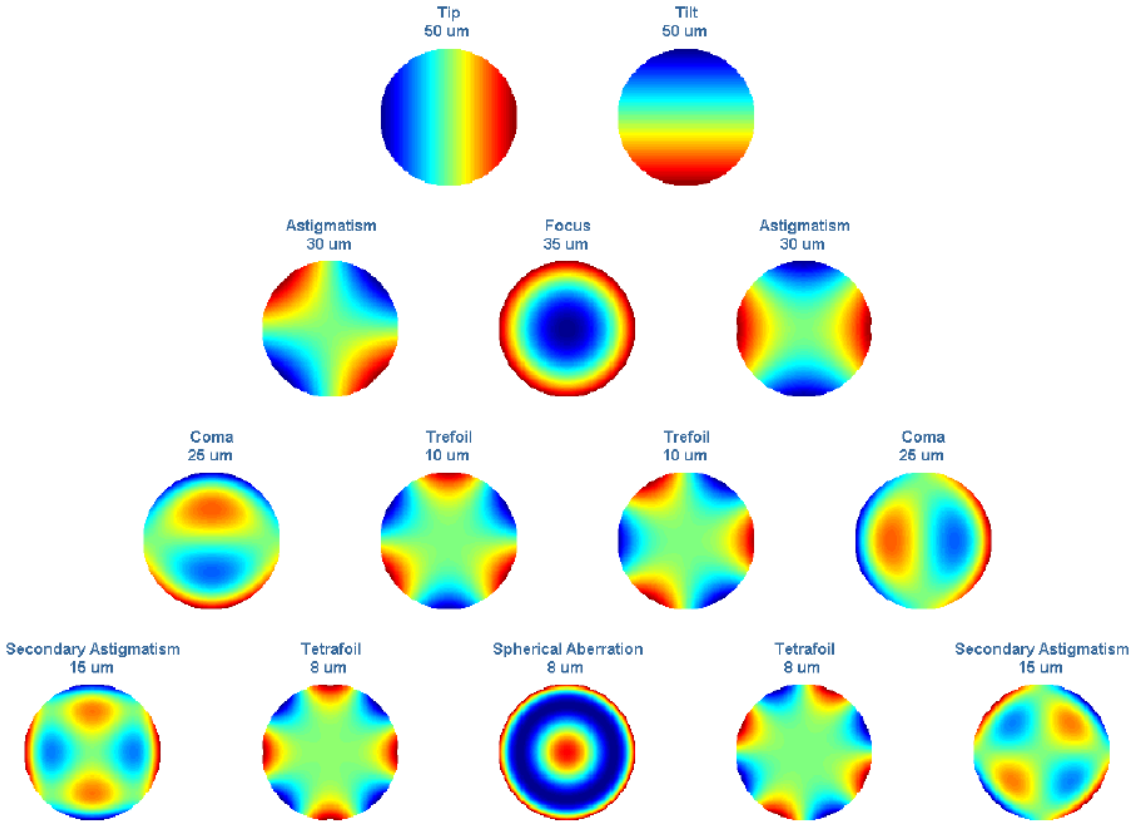

Figure 27 - Maximum wavefront displacement of the DM depends strongly on the type of shape (Photo courtesy of ALPAO).

The major performance parameters of the DM, and its drive electronics, are given in Table 5.

DM52 – DE64 Technical Specifications	Value	Unit
Max Actuator Stroke	25	um
Max Tip/Tilt Wavefront	50	um
Max Defocus Wavefront	35	um
Number of Actuators (N)	52	-
Range of Voltage Output from PC (V)	±0.5	V
DM Drive Electronics DAQ Resolution	14	Bits
Closed-Loop DM Bandwidth	>200	Hz

Table 5 - Specifications for the DM52 deformable mirror and DE64 mirror drive electronics

The accuracy of the deformable mirror is specified with two error terms, the fitting error and shape error. The fitting error is the difference between the desired shape and the optimal shape given the fixed number of actuators. The shape error is the difference between the optimal shape and the measured shape after the DM is commanded. When integrated with a closed loop control system, the DM can attain a surface flatness of 10 nm RMS.

Chapter 3 – Design and Implementation of the AO Controller

The control system has two roles: (i) manipulation of the wavefront to position the trap in the desired *x*,*y*,*z* position, (ii) correction of aberrations caused by drift and misalignment by interpreting the trapping laser's wavefront and making adjustments to the DM shape. In both cases, the DM adjustment made by the control system is based on wavefront sensor measurements. In order to relate WFS measurements to DM commands, a calibration is performed. During calibration, the WFS measurements for specific DM shapes are recorded. These results are then inverted, allowing DM commands to be generated to form the desired wavefront. This section details how the control system fulfills these two roles using digital control theory.

Adaptive Optics Control Theory

Closed loop wavefront control is one of the innovative features of this optical tweezers system. A flow chart, showing the functional components of the apparatus, is given in Figure 28. The control system is labelled "WFS-DM controller", and its interfaces with the system are given in bold print. The interface labels in Figure 28 (bracketed items) are employed throughout this chapter.

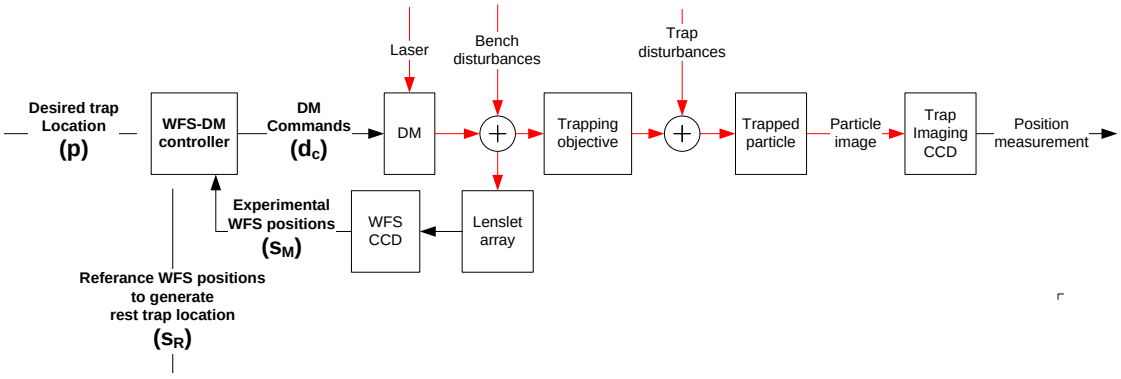

Figure 28 - A flow chart illustrating how the optical trapping system moves from a desired trap location, to the measured trap position. In bold are the interfaces to the WFS-DM controller. Red lines represent optical parameters and computer signals are shown using black lines.

The controller has one output, DM commands d_c, and three inputs; experimental WFS positions s_M, reference WFS positions s_R, and desired trap location p. The DM command output specifies each DM actuator voltage, which is communicated to the DM control electronics. The input labelled reference WFS positions s_R, contains the x,y pixel locations of each lenslet focus when the trap is at its rest/home position. They also correspond to the WFS positions when all wavefront error is removed. The second input is labelled experimental WFS positions s_M. These are the WFS lenslet focus positions formed by sampling the actual laser beam, after its wavefront is shaped by the DM. This input is the WFS measurement.

In reference to the controller's second role of removing wavefront error, the WFS sends DM commands d_c to make the WFS measurements s_M match the reference WFS positions s_R.

In the controller's primary role of manipulating trap position, the controller uses the desired trap position input p to generate an offset to the WFS pixel locations s_D (not shown in Figure 28), that is added to the reference WFS positions s_R. Through a process of calibration, it is known that when the WFS measurements s_M equal the sum of s_D and s_R, the trap will be at the desired location. The controller then sends DM commands to make the WFS measurements s_M match this sum.

Deformable Mirror - Wavefront Sensor Control Loop

Three axis control of the trapped particle is accomplished using the DM, WFS, and trap imaging CCD. When the controller is calibrated, the user can command the trap to a particular *x,y* location. This causes the controller to change the DM shape, thereby moving the trap. The controller is also able to move the trap in the *z* direction; however, since there is no '*z*' position sensor, the *z* movements are not calibrated in terms of true position in the trapping chamber. Instead, WFS offsets s_D are generated using the Zernike definition of defocus (Figure 10).

Trapping location – WFS - DM Controller block diagram

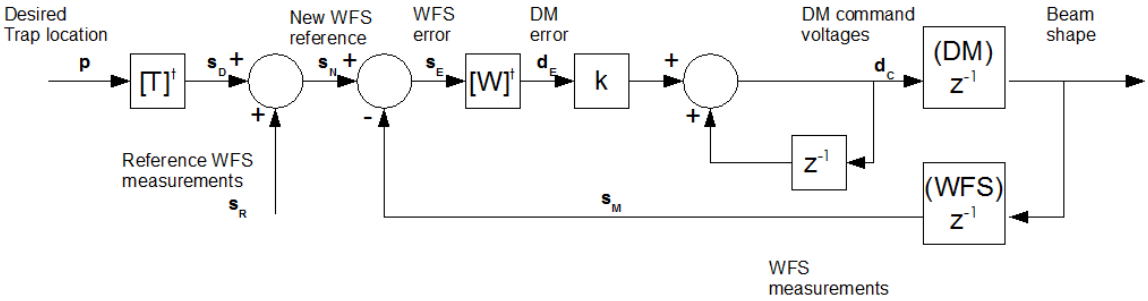

Figure 29 - The discrete representation of the controller shows how a desired trap location is converted into DM command voltages. The DM and WFS are modeled as single delays, z^{-1} in control terms.

The discrete representation of the controller is given in Figure 29 (this diagram was represented as the "WFS-DM controller" block in Figure 28). The trap controller's working method is described below, with reference to the terms defined in Figure 29.

The controller receives a software input from the user representing a desired trap position, *p*. This position is in terms of pixel co-ordinates on the CCD looking at the bright-field image of the trapped bead. This position is converted to a vector of WFS centroid position offsets s_D, by multiplying *p* by the command matrix, T^t, which is the pseudo-inverse of the Trap-WFS interaction matrix *T*. The interaction matrix *T* is a 104x2 element matrix, determined through a calibration process detailed in a following section. Generally, it measures the relationship between trap position and wavefront sensor measurements.

Based on the desired trap location *p*, the WFS offset vector s_D is added to the reference vector s_R , forming a new WFS reference vector s_N. The controller's goal is to manipulate the DM such that the WFS centroid measurements, s_M, match this s_N. The WFS vectors (s_D , s_R , s_N , s_E and s_M) contain *x* and *y* position data for each lenslet focus. Since 52 lenslets are used here, each WFS vector has 104 elements.

The error between s_N and the current vector of WFS measurements s_M forms the WFS error vector s_E. A vector of DM voltages d_E, which will remove this error, is calculated by multiplying s_M by the command matrix $W^{\dagger}$, which is the pseudo inverse of the WFS-DM interaction matrix *W*. The interaction matrix *W* contains WFS measurements caused by moving each DM actuator individually. Creating the matrix *W* is described in the section on WFS-DM calibration. A gain *k* is multiplied by the DM voltages d_E and the resulting vector is added to the current voltages, forming a new voltage vector d_C. The loop adding d_C to d_E forms an integrator, which means the DM commands grow until the error is removed. These voltages are sent to DM control electronics via a serial cable which deforms the DM, changing the wavefront. The process begins again with the next execution of the control loop, beginning with a new vector of wavefront measurements s_M. The controller is stable for gains up to 1.2, allowing the controller to react quickly to changing conditions.

Calibration of the Relationship between WFS Measurements and DM Commands

The goal of WFS-DM calibration is to produce a command matrix W^t that, when multiplied by a vector of desired WFS measurements *s*, gives a vector of the required DM voltages commands *d*. This is done by finding the inverse of a matrix which can easily be determined through a simple calibration process, the interaction matrix *W*. Each column w_i of *W* is calculated by applying a voltage *h* to single actuator d_i and recording the WFS measurements s_i ; where *i* refers to the particular actuator being moved. This is repeated until each actuator has been moved. Put simply, each column of *W* contains the change in WFS measurements when a particular DM actuator is moved. Therefore, *W* is an *m* by *n* matrix where *m* is the twice the number of lenslets, representing the *x* and *y* positions of the lenslet foci, and *n* is the number of DM actuators. The form of *W* is given in (10), note that dividing by WFS measurements *s* by applied DM voltage *h* normalizes *W* with respect to DM voltage.

$$W = \left[\frac{s_1}{h} \quad \frac{s_2}{h} \quad \frac{s_3}{h} \ldots \frac{s_{i=n}}{h} \right]_{mxn} \qquad (10)$$

A vector of WFS measurements *s* is related to *W* and the DM vector *d* by $Wd = s$. However, the controller needs to determine the DM vector *d* that produces measurements *s*. It would be nice if *W* could simply be inverted, however it is not a square matrix. The inverse is $n_x m$, where in this case $m = 2n$, which is to say the inverse has twice the number of equations (WFS measurements) as unknowns (DM actuators). Since the matrix is not strictly invertible, a technique called singular value decomposition (SVD) is used to calculate the so called pseudo-inverse of *W*, labelled W^t. The pseudo-inverse has

the effect of applying a least-squares-fit to the over-determined inversion problem. The SVD uses three matrices U, Σ , and V^T, the product of which equal W. This is shown in equation (11).

$$W = U \sum V^T \tag{11}$$

Using the definition of the pseudo-inverse, $W^{\dagger}$ is given by equation (12).

$$W^+ = V \sum^+ U^T \tag{12}$$

Where $U_{m,m}$ and $V_{n,n}$ are orthonormal and $\Sigma_{m,n}$ is matrix containing only diagonal elements, σ_i, equal to the singular values of W. Calculating U, Σ , and V^T is computationally difficult, in this experiment a built-in Matlab command was used with the syntax: [U, Σ, V] = svd(W). The matrix $\sum^+_{m,n}$ is simply $\Sigma_{m,n}$,where the values σ_i have been replaced by $1/\sigma_i$. Small values of σ_i represent sets of DM shapes that produce wavefronts which are difficult to detect on the WFS. These small singular values, which would result in correspondingly large values in $\sum^+_{m,n}$, are replaced by zeros in $\sum^+_{m,n}$ to avoid putting shapes on the DM that would have a poor signal to noise ratio.

Having calculated W^+, a desired set of WFS measurements s can be produced by outputting a DM voltage vector d, calculated using equation (13).

$$d = W^+ s \tag{13}$$

The calculation of W and W^+ does not have to be done while the controller is running; it is only done once during calibration.

Calibration of the Relationship between Trap Position and WFS Measurements

At each execution of the control algorithm, a set of DM voltages d is calculated based on the WFS-DM command matrix W^{+}, and the WFS error. The WFS error is the difference between WFS measurements s_M, and the sum of the WFS reference positions s_R and the WFS offsets s_D. The equation overall equation is given in (14).

$$d = W^{+}\left(s_M - s_R - s_D\right) \qquad (14)$$

The WFS offsets s_D, control the position of the trap. The offsets are calculated using equation (15), where p is the desired trap position and T^{+} is the trap position command matrix.

$$s_D = T^{+} p \qquad (15)$$

The remainder of this section details the process of calibration required to determine the trap position command matrix T^{+}, from an interaction matrix T.

The interaction matrix, T, was determined by relating trap position to WFS offsets corresponding to the Zernike mode of tip/tilt. Tip/tilt is seen on the WFS as an offset of an equal amount to each WFS lenslet's focal position. Procedurally, a bead was first trapped, and then a WFS offset s_D was added to the reference s_R which contained an equal offset for each lenslet. The controller was then activated, causing the DM to change such that the WFS measurements s_M matched the sum of the WFS offset and reference. This causes the trap to move, and the new x,y trap position is recorded. This process was repeated; changing the WFS offset s_D to move each lenslet in a rectangular spiral pattern,

corresponding to various strengths of tip/tilt. The pattern is necessary because large changes in wavefront reference will cause the trap to be lost, as the DM makes large movements moving the laser outside the extent of the trap. The picture in Figure 30 shows the rectangular grid pattern for a single WFS lenslet centroid, note however that each lenslet was actually moved together through this pattern.

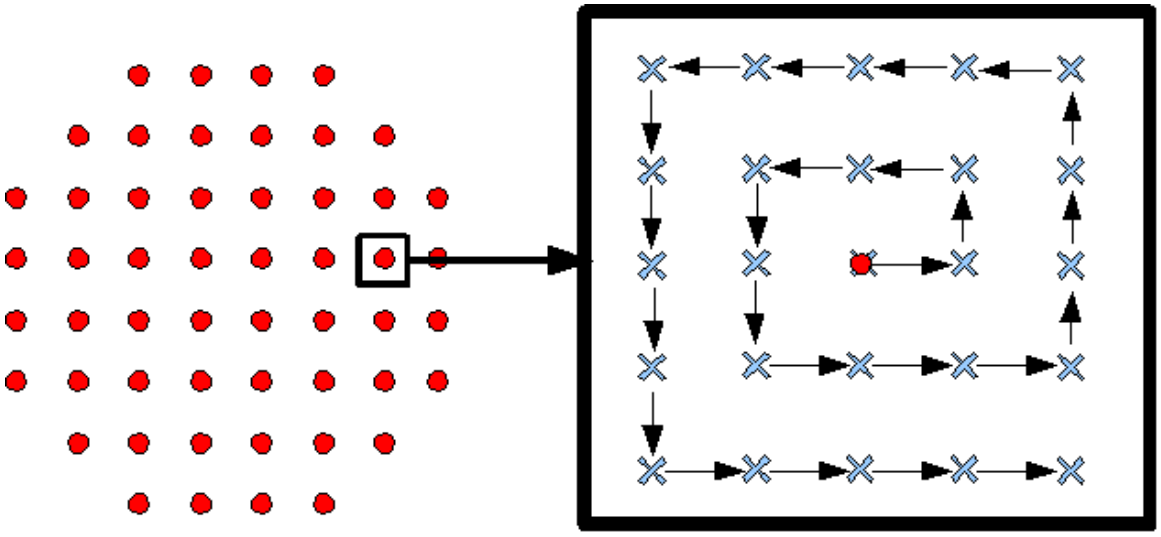

Figure 30 – WFS lenslet centroids are shown in red (left), each was moved together in a rectangular grid pattern (right) while a bead was trapped (not shown). After each movement the position of a trapped bead was measured. This was done to calibrate the relationship between WFS measurements and trap position. This corresponds to calibrating the trap position using the Zernike definition of tip/tilt, which is sensed as equal offsets in WFS centroid position.

The result of this calibration is the interaction matrix T converting wavefront measurements s_M to trap positions p. A least-squares-fit line was calculated for each lenslet's vector in T. Each slope was inverted giving a value which converts trap position p to a particular lenslet's centroid measurement s_i. The result is the matrix T^+ that when multiplied by desired trap position p gives the required WFS offset s_D.

Removal of Static Aberration

The controller is also used to remove the static wavefront errors created by misalignment and lens aberrations. The wavefront sensor was employed to measure the static wavefront error. This wavefront error, in terms of centroid displacements, was then converted into the set of 21 Zernike polynomials given in Figure 10. The magnitudes of the Zernike polynomials are plotted in Figure 31.

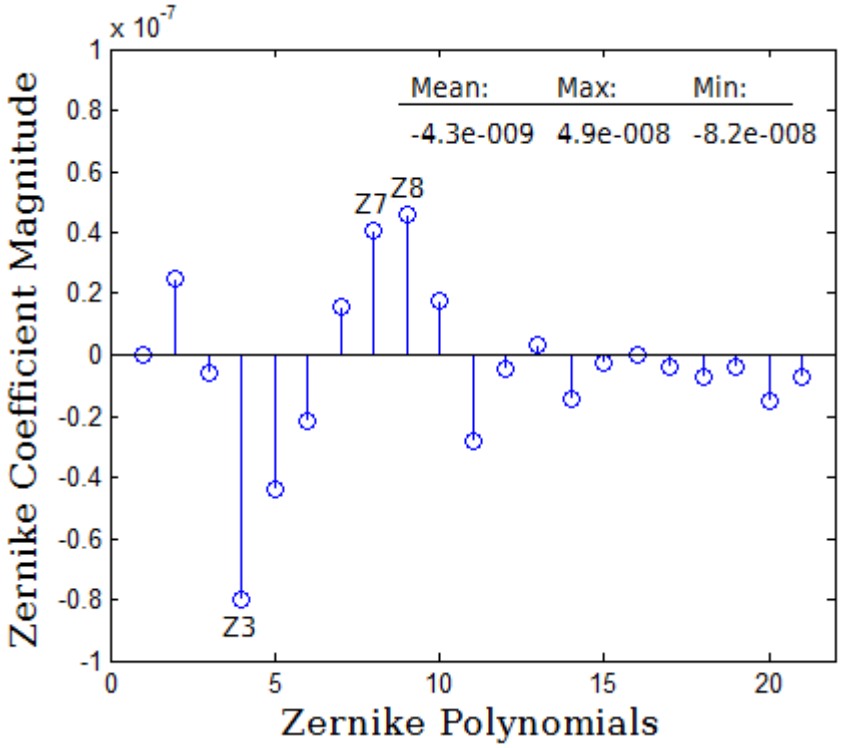

Figure 31 – Zernike mode representation of the static wavefront error of the optical system

The largest Zernike mode is defocus, Z3, followed by astigmatism, Z7-8, and the first coma, Z5. The controller was then activated to flatten the wavefront. The resulting wavefront was again measured using the WFS, and fit with the Zernike polynomials. The Zernike coefficients corresponding to the corrected wavefront are given in Figure 32.

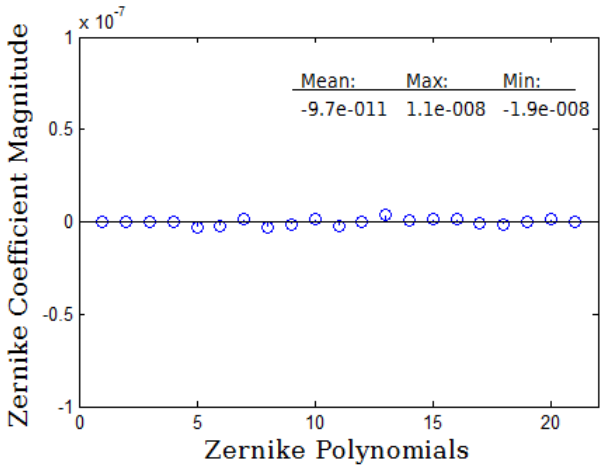

Figure 32 – Zernike representation of the wavefront error with the AO controller activated

With the controller activated the Zernike coefficients show that the wavefront error has been dramatically reduced. The mean coefficient magnitude has dropped by approximately two orders of magnitude. This reduction shows that the controller has been properly calibrated and is functioning well.

Minimizing the Non-common Path Error of the Wavefront Sensor Optics

The DM is run in closed loop, therefore the system continually minimizes the wavefront error up-beam from the trapping objective. Similarly, the DM will erroneously compensate for wavefront error caused by misalignment between the lens pair resizing the beam to fit the WFS lenslet array. This error is minimized by selecting a lens pair with long focal lengths, which minimizes the affect of misalignment on the wavefront. Also a portable wavefront sensor (HASO v3) was used to check that the difference between the wavefront before and after the WFS optics was negligible.

Chapter 4 – Determination of Trap Stiffness

Employing the optical tweezer as a force probe is an important use of the device. It is difficult to apply piconewton scale forces using other techniques. This allows biophysicists to carry out ground breaking research in molecular biology. A key parameter of a force probe optical tweezer is trap stiffness. Force is not directly measured using the optical tweezer, instead it is related to trapped particle displacement through the trap stiffness. Therefore, determining the trap stiffness is key to the development of a force measuring probe. Currently, the most accurate method for determining trap stiffness is the use of interferometry [23]. Unfortunately, this technique is not well suited for the particles used in this experiment which are much larger than the laser's wavelength. The technique has not been successfully scaled to multiple trap systems, which is the future direction of apparatus development. Instead, video analysis of bead position is used to determine trap stiffness.

The Stokes Drag Method for Determining Trap Stiffness

In this technique, a known force, created by a moving fluid's drag, is applied to the trapped particle causing it to be displaced slightly. It has been shown [33], that for small particle displacements (relative to particle diameter) the displacement is proportional to the applied force. The linear spring equation (16) is an accurate model of the trap's force-displacement behaviour.

$$F = -kx \qquad (16)$$

Where, F is the trap's restoring force opposing the bead displacement, k is the trap (or spring) stiffness, and x is the observed displacement of the trapped bead from its nominal position. Stiffness is calculated by dividing the applied force by the measured displacement.

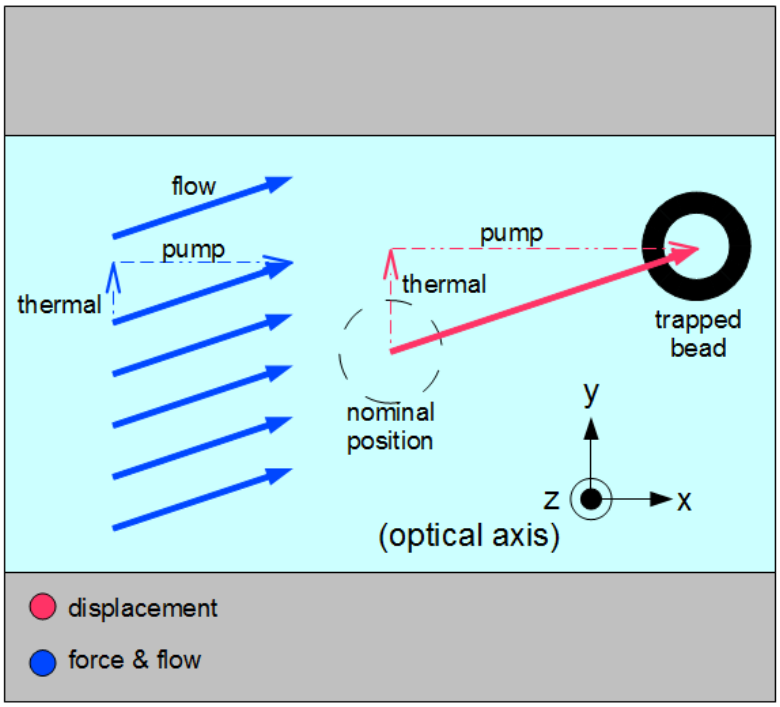

Figure 33 - Fluid flow (blue) due to pumped flow and thermal circulation applies force to a trapped bead. The bead displaces in the same direction as the applied flow (red). The displacement is linearly related to the flow velocity and the stiffness of the optical trap.

To create a displacement x, a force is applied due to fluid drag created by water flowing perpendicular to the optical axis. In this apparatus, fluid flow is created by a pressure pump and by free convection due to laser absorbance of the water. This convection acts against gravity, perpendicular to the applied flow, as shown in Figure 33. In equilibrium,

the drag force is opposed by the trapping force given by (16). Ignoring inertial considerations, the drag force imparted on a body is given by equation (17).

$$\boldsymbol{F} = -b\boldsymbol{V} \qquad (17)$$

Where $\boldsymbol{F}$ is the force vector, $\boldsymbol{V}$ is the vector of relative velocity, and b is a drag constant. Because $\boldsymbol{F}$ is related to $\boldsymbol{V}$ by a constant, the x and y components of force and velocity can be calculated independently. For laminar flow over spheres, Stokes showed that the drag constant is given by the simple expression in (18).

$$b = 3\pi\eta d \qquad (18)$$

Where, η is the dynamic viscosity of water, and d is the sphere diameter. Often, the optical trap is positioned 10 (or less) bead diameters from the window of the trapping chamber. In this case, the above drag coefficient must be adjusted to reflect interaction with the window surface [1], however this experiment does not require such adjustment. By substituting (18) into (17), and setting the result equal to (16), the trap stiffness is given by (19) below.

$$k = \frac{3\pi\eta dV}{x} \qquad (19)$$

Stokes' equation ignores the drag force required to change the momentum of the fluid as it flows over the bead. The equation only models the fluid's friction due to viscosity. In fluid flow the Reynolds number gives the ratio of magnitude of inertial over viscous forces. For Reynolds numbers < 1, Stokes equation gives very good results. This experiment is well within this range, the Reynolds number varying here between 1E-4 and 1E-6. The equation for Reynolds number is given below in (20).

$$Re = \frac{2Vr}{v} \qquad (20)$$

Here, *V* is the flow velocity, which in this experiment ranges between 1E-5 and 1E-7 m/s, and *v* is the kinematic viscosity of water, equal to 0. 9E-6 m^2/s at room temperature. The beads used here have a radius *r* equal to 5E-6 m.

Calculating the Time Required for a Free Particle to Reach Bulk Velocity

The method used here to determine flow velocity is based on the assumption that when fluid is flowing, the difference in position of a non-trapped particle multiplied by frame rate (1/s) gives the velocity of the fluid. In other words the particle accelerates instantaneously to match the flow velocity, when sampling at the CCD's frame-rate. As a check, the following calculation gives the time required to accelerate a 10 um particle to 99.99% of the flow velocity (21).

$$F = -b\mathrm{V} = \mathrm{m}\frac{\mathrm{dV}}{\mathrm{dt}} \qquad (21)$$

Integrating gives the result in (22).

$$-\frac{b}{m}t = \ln\mathrm{V} + \mathrm{C} \qquad (22)$$

Solving for *V*, and noting that $V(t=0) = V_f$, where *V* is the velocity of the fluid relative to the bead and V_f is the velocity of the fluid relative to the flow chamber, gives the expression in (23).

$$V = \mathrm{V_f}e^{-\mathrm{tb}/\mathrm{m}} = \mathrm{V_f}e^{-\mathrm{t}6\pi\mathrm{vr}/\left(\frac{4}{3}\pi\mathrm{r}^3\rho\right)} \qquad (23)$$

Solving (23) for *t* and using the 99.99% condition by setting $V/Vf = 0.0001$, *r*= 5E-6 (m) , *v* = 1E-3 (Pa*S), and density *p*= 1050 (kg/m^3) gives *t* = 1E-4 seconds. This is approximately 3 orders of magnitude faster than the frame time (1/15 Hz). As the

particle reacts much faster than the framerate, the displacement across frames is used as an indicator of the flow velocity.

Experimental Setup for the Stokes Drag Method

Applying the Stokes Drag method requires the experimental evaluation of the following variables:

- d, bead diameter (m)
- V ,fluid velocity (m/s)
- x, trapped bead displacement (m)

A description of how each variable is determined is discussed below.

Measuring Trapped Bead Diameter While Trapping

The Stokes drag component of the stiffness measurement depends on the diameter of the trapped particle. Therefore, the ideal scenario would be to measure the diameter of the trapped particle. This is challenging because the extent of a trapped bead is difficult to measure using the imaging CCD. A trapped particle is shown at different trapping depths in Figure 34.

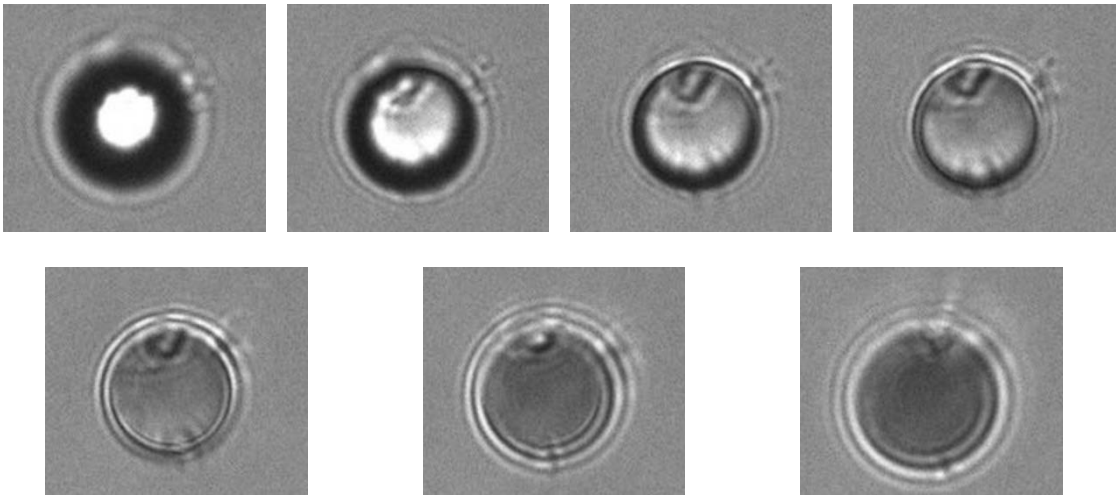

Figure 34 - Seven images of the same 10 um bead at different depths along the optical axis. The diameter appears to change slightly through the focus. Several particles are seen to be stuck to the bead, at approximately 12:00, 2:00 and 6:00

The sharpest image is the top-right image. However, the exact extent of the bead is difficult to identify given the diffraction effects near the edge. Therefore, the manufacture's specified particle size was confirmed for several beads and the bead diameter was not measured during trapping. The dimensions of the polystyrene beads (Polybead – Polysciences Inc.) are given in Table 6.

Nominal Diameter:	Mean Diameter:	Standard Deviation:
1 um, ± 1%	1.025 um	0.01 um
6 um, ± 3%	5.497 um	0.168 um
10 um, ± 5%	9.977 um	0.412 um

Table 6 - Polystyrene bead dimensions (Manufacture data)

The diameters were measured by placing the beads on a microscope slide and using a precision microscope equipped with a digital readout accurate to 0.1 um. The measured diameters of the 6 and 10 um beads were found to be within a standard deviation of the

mean given by the manufactures specifications. The 1 um beads were measured to be approximately 1 um, but the microscope device did not have the precision necessary to confirm the standard deviation.

Frequently rod shaped materials were stuck to the trapped beads. This can be seen in Figure 34. The likelihood of material being stuck to a bead increased with the amount of time the beads were left in the needle. Extra particles on a streaking bead cause no issues with the velocity calculation, but they can influence a trapped particle. It has been shown [35] that foreign material bound to a trapped bead can significantly influence the observed stiffness due to an increase in the drag coefficient. Therefore beads with stuck on material were avoided.

Experimental Determination of Fluid Velocity Based on a Streaking Particle

The fluid velocity must be calculated in order to determine the drag force term of the stiffness equation. Fluid velocity was observed indirectly by tracking the change in position of a free particle streaking across several frames. The velocity is determined from the displacement and framerate. The expression used to determine velocity is given in (24).

$$V = \frac{\vec{a}_{f,N} - \vec{a}_{f,1}}{N} fm \qquad (24)$$

Vectors $\vec{a}_{f,N}$ and $\vec{a}_{f,1}$ represent the pixel position of a point on the streaking bead in the final and initial frame respectively. Experimentally, the *y* component of bead centroid was ignored for reasons discussed later in this chapter. The other terms in (24) are the

frame rate *f*, the number of frames *N* between the initial and final particle position, and a conversion factor *m* between imaging CCD pixels and meters.

To calculate trap stiffness several minutes of video frames were captured, from which both fluid velocity and trapped-particle displacement were determined. During the recording, the flow speed was set to a variety of speeds. Afterwards, a plot was created showing the centroid of the trapped bead through the video. Because the trapped bead's location changes with the flow speed, areas of constant location correspond to steady flow rates. A centroid plot in Figure 35 shows a region of relatively steady flow in the centre of the plot.

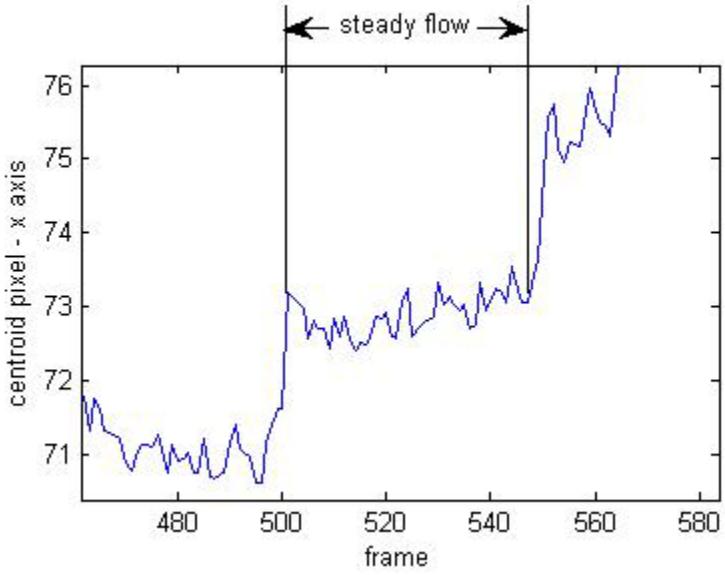

Figure 35 - Trapped bead centroid showing section of steady flow rate

The frames nearest to the start and end of the region of steady flow containing a streaking particle usable to determine flow velocity were used to determine $\vec{a}_{f,N}$ and $\vec{a}_{f,1}$ in the velocity equation (24). The positions, $\vec{a}_{f,N}$ and $\vec{a}_{f,1}$, were determined through manual examination of the two frames. The estimated error of this technique is ±0.24 um, based on repeating the measurement several times.

An example of measuring the streak distance is given in Figure 36. For illustrative purposes the displacement is small. Typically displacements ranged between 50 and 100 pixels.

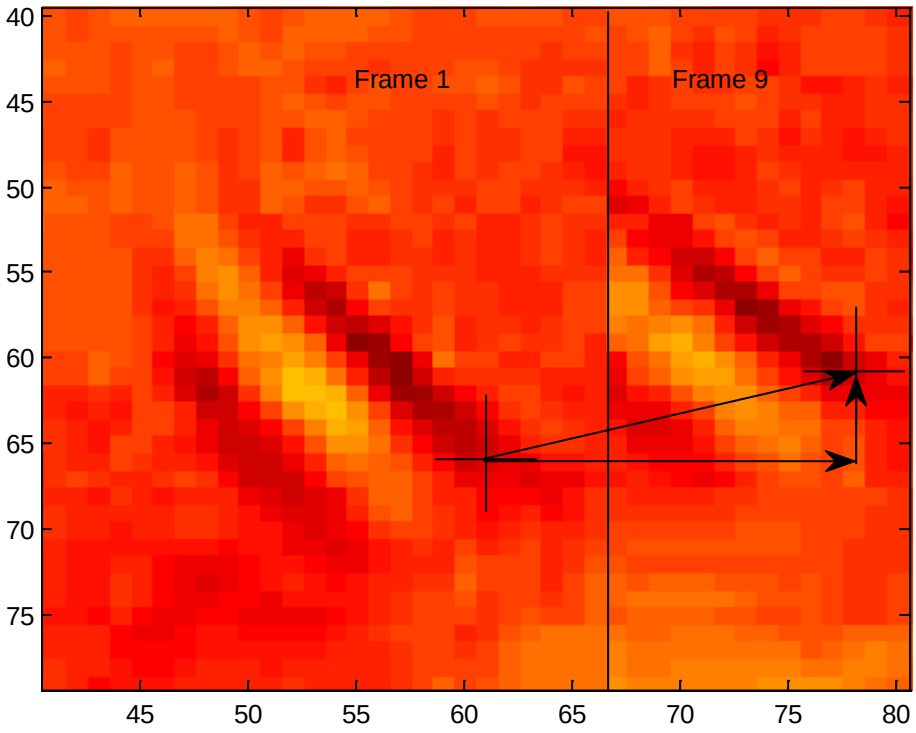

Figure 36 - Two frames of the same scene have been stitched together and depict a particle moving due to the presence of water flow. The relative motion of the particle was determined manually by observing the change in position of a particle feature with good contrast. The particle here was found to have moved 17 pixels in 9 frames at a frame rate of 2fps, corresponding to a flow speed of 0.45 um/second. (0.119 um/pixel)

The figure shows a small segment of the total frame. The contrast ratio between particle and background is not high, and the particle's area small, so a simple centroiding algorithm would not be well suited to determine the change in position of the trapped particle. The wide range of particle shapes and sizes would also make it difficult to use a matched-filter.

Experimental Determination of Trapped Bead Displacement

Changes in bead position, due to an applied flow, are used to determine the trap stiffness. Changes in position are an important measurement, often limiting the sensitivity of the optical trap as force probe. To determine the bead position, a centroiding algorithm was used to calculate the center of intensity of the bead's image in terms of pixels in the overall frame.

Relative to the no-flow position of the trap, the 2D trap displacement is calculated using (25).

$$\vec{x} = \frac{1}{k}\vec{F} = \frac{b}{k}\vec{V} = \frac{b}{k}\left(p(t)\hat{x} + q(\mathrm{P})\hat{y} \right) \qquad (25)$$

Pumped fluid flow is specified as a function of time, *p(t),* and is idealized as acting only in the $\hat{x}$ direction. When trapping with optical powers larger than 12mW (measured at the back aperture of the trapping objective), significant fluid flow in the upward direction was observed due to local heating of the water. This flow is given as a function of laser power $q(\mathrm{P})$, and was observed to act in the y direction.

A plot of *x* and *y* positions of a trapped particle subject to increasing flow velocity is given in Figure 37.

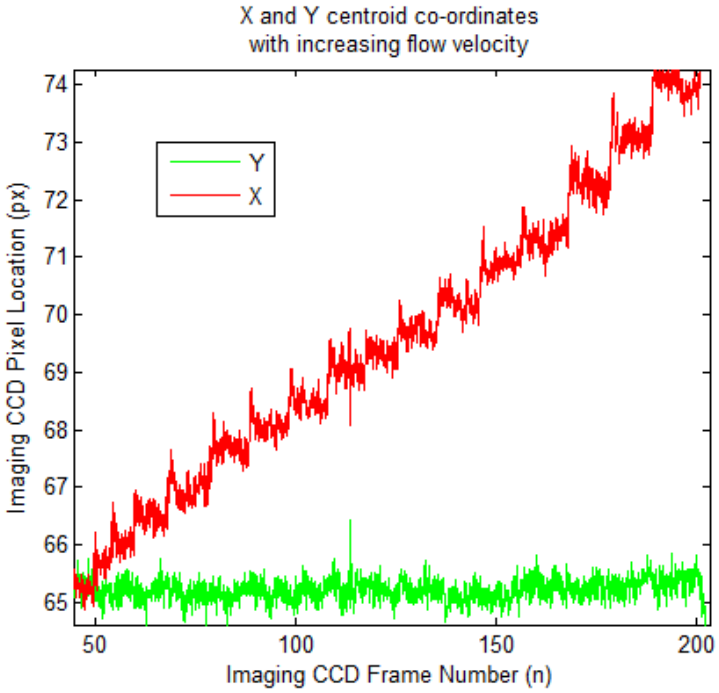

Figure 37 - A trapped bead's x and y position is measured while being subjected to flow at progressively larger velocity. The position is observed to change in the x direction only, meaning the flow direction is well aligned with the x co-ordinate of trap position.

Position measurements were more consistent using only the *x* component of the centroid. Displacements due to pumped flow in *y* are small in comparison to the random thermal fluctuation of the trap.

The trap displacement was calculated by subtracting the average *x* component of the trapped bead's centroid over *N* frames from the no-flow *x* co-ordinate of trap position. The calculation is given below in equation (26).

$$x = m\frac{\sum_{i=1,N}|a_{b,i}-a_{f,o}|}{N} \qquad (26)$$

Where N is the number of frames, the no-flow centroid is given by $a_{b,o}$, the calculated centroid of a given frame is $a_{b,i}$, and the conversion from pixels to meters is given by m.

Enhancement of the Trap Position Image to Improve Accuracy

The trap position calculation accuracy was improved from the application of image enhancement techniques to a sequence of CCD images. To calculate the centroid, a region of interest (ROI) is defined large enough to view the trapped particle as it is displaced by the applied flow. A raw CCD image of a bead in the ROI is shown on the left of Figure 38. The dark circular region (blue) is the bead surrounded by a lighter background. The magnitude of the pixel intensities in the raw ROI is reversed so the trapped bead becomes light and the background dark (centre of Figure 38). Noise in the centroid measurement was reduced by thresholding the image to eliminate the background (right Figure 38).

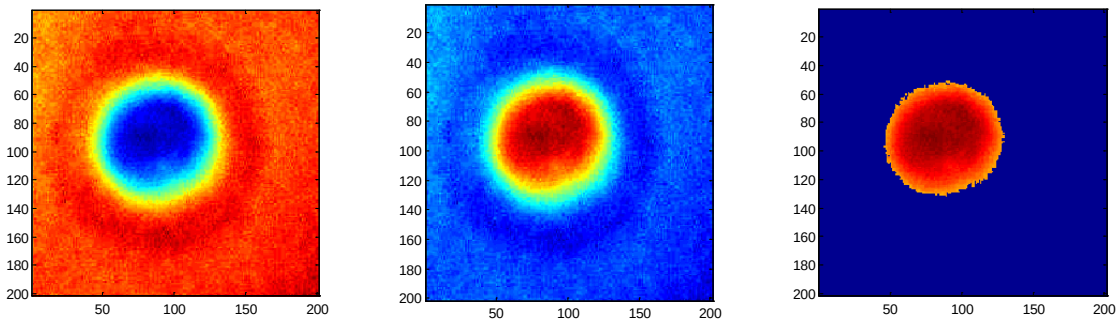

Figure 38 - Three images of a single frame of a 10um trapped particle. Low intensities are shown in blue, and the highest intensities in yellow. The left image is raw, the trapped bead has lower intensity than the background. The centre image has been rotated by intensity. The right image has been had a threshold applied to eliminate the background, the centroid will be calculated from this image.

Errors in the centroid measurement are mainly due to the elimination of pixels as a result of thresholding, fluctuations of the light source, and the electrical noise of the imaging CCD. The trap displacement measurement error includes the centroid measurement error, and other sources such as thermally induced motion, drift of the trapping chamber/objective position, drift of the positions of other optical components, and fluctuations of the air surrounding the bench.

A study was done to determine an appropriate threshold. A 10um bead was trapped and 100 frames were captured. A sample frame showing the trapped particle before thresholding is given in Figure 39.

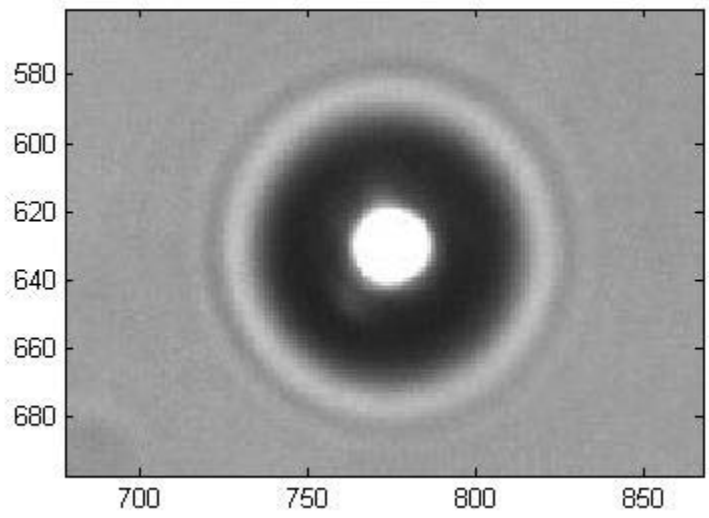

Figure 39 – 10um bead used to determine an effective threshold, units in pixels

Using these 100 frames, the centroid was calculated for a range of thresholds between 0 and 180, out of a possible 255. For each threshold, the standard deviation of bead centroid was calculated, the results for a threshold between 50 and 180 are plotted in Figure 40.

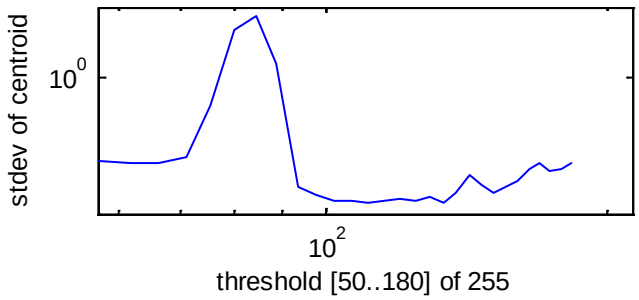

Figure 40 - Threshold values were varied between 50 and 180 of a possible 255 levels (8-bit image). The standard deviation of the centroid is plotted on the y axis.

Thresholding was shown to greatly affect the standard deviation of the centroid. The threshold minimizing uncertainty is given in Table 7.

Number of Frames	Best Threshold – [0..255]	Centroid Uncertainty Due to Imaging – (um)
100	**[100..135]**	0.0067

Table 7 - Threshold value minimizing trap position uncertainty

Chapter 5 - Characterization of the Optical Tweezer System

The functionality of the prototype optical tweezer apparatus was investigated to determine its advantages and limitations. Using the apparatus as a force probe requires determining trap stiffness, and its sensitivity is dependent on the accuracy of the trap position detection algorithm. These parameters are investigated and will be used as benchmarks to guide design refinement. The AO system's ability to manipulate particle position is also investigated.

Imaging CCD Pixel Scale, Field of View, Resolution and Framerate

The imaging CCD provides a microscope image of the trapping chamber. In order to measure the position of the trapped particle in real units, the scale converting image pixels to microns was determined. Pixel scale was determined by placing an object of known size, a needle, in the trapping plane and counting how many pixels it measured across. The pixel scale is given in Table 8.

Gauge (um)	# CCD Pixels (px)	Imaging CCD Pixel Scale (um/px)
84	706	0.119

Table 8 - Imaging CCD pixel scale

The field of view, framerate, and resolution of the imaging system are given in Table 9.

Framerate (fps)	Resolution (*x* px, *y* px)	Field of View (*x* um, *y* um)
15	1600, 1200	190, 140

Table 9 - Imaging CCD framerate, resolution and field of view

Observed Flow Velocity Induced by the Absorption of Laser Light

The trapping chamber is several millimetres deep. This atypical depth causes more laser light to be absorbed by the water than in most optical trapping apparatus. This heating induces a flow in the *y* direction, with a velocity related to the optical power at the trap. The flow velocity was measured at several optical powers and is plotted in Figure 41.

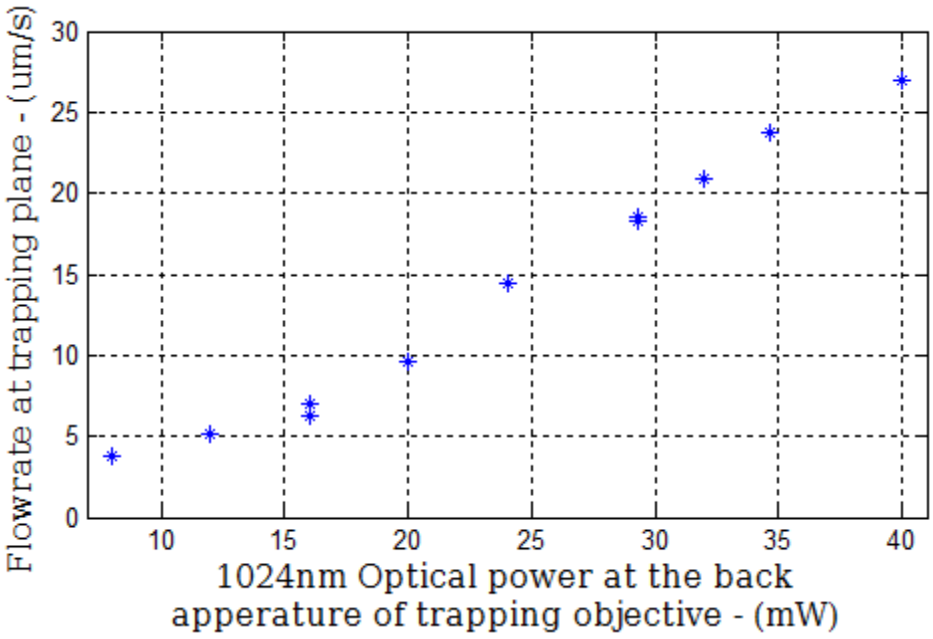

Figure 41 - Flow velocity caused by absorbed laser light in the trapping chamber

This flow velocity was measured with the trap at a fixed distance from the wall of the chamber. When the trap was moved closer to the wall, the flow velocity decreased.

Accuracy of Trap Position Determination

As discussed in Chapter 4, the trap position measurement is subject to errors created by the random Brownian motion, and also by errors in the image processing methodology. The standard deviation of the trap position measurement was used to determine the

experimental accuracy. A 10 um particle was trapped using 12mW of optical power and its rest position was measured for each of 300 hundred frames. The standard deviation of the centroid in *x* and *y* was 0.041um and 0.042um respectively. The magnitude of the standard deviation due to thermally induced Brownian motion is influenced by trap stiffness and decreases with increasing trap stiffness.

Compensating for Trap Position Drift Using the AO System

The optical components are rigidly mounted to the optics table but are subject to slight changes in position over time. This variation causes the trap position to drift over larger period of time. Drift degrades the ability to use the optical trap as a force probe because it affects the observed trap displacements. Drift due to moving optical components before the trapping objective should be correctable by the AO system. Note that moving optical components cause many forms of wavefront error, however it is the tip/tilt component of total error that causes drift in trap position. A test was done to measure how much drift could be removed by comparing the drift in tip/tilt WFS measurements in open vs closed loop.

Over the period of an hour, the WFS was used to measure the laser wavefront's Zernike modes of tip/tilt with the controller turned off. The relationship between tip/tilt measurements, and trap position, was used to convert the tip/tilt modes trap position drift. The controller was then activated, and again the WFS's Zernike modes of tip/tilt were converted to drift in trap position. The results are shown in Figure 42.

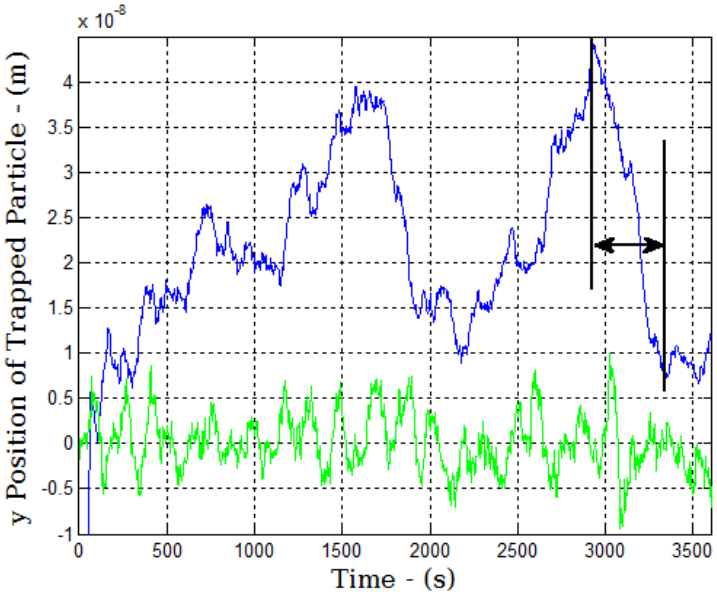

Figure 42 - Drift of the optical trap, due to the movement of components before the trapping objective, deduced from WFS measurement of tip/tilt. With the AO system deactivated, blue trace, significant drift is observed. A segment of the trace, black arrows, was used to calculate a 0.050 um/min representative rate of drift. Activating the AO system, green trace, contains the drift to a range of approximately 0.01 um.

The plot shows the open loop drift in trap position in blue, and the closed loop drift in green. When the loop is closed, the trap position is kept within a range of 0.01 um. The segment of the open loop plot between the black arrows was used to calculate a 0.050 um/minute representative rate of drift.

Another experiment was done to determine the residual drift in trap position, caused by motion of the trapping objective and chamber. A bead was trapped and its position monitored over time with the AO system activated (Figure 43).

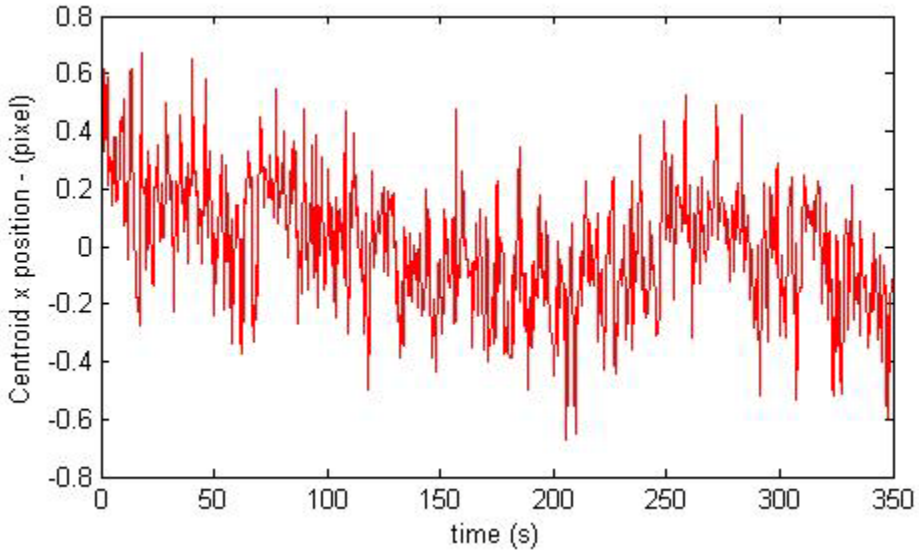

Figure 43 - Trap position measured using the imaging CCD, of a 10 um bead, showing significant drift

Observing the centroid position in Figure 43, the magnitude of the remaining drift is approximately 0.02um (0.17 pixels) per minute. The remaining drift is due to movement in the objective mount, which is not corrected for by the control loop.

Spatial Range of the Optical Trap

The spatial range of controllable trap position determines both the overall particle movement and the required initial proximity, of a particle to be trapped, to the nominal trap position. The measurements were made by calculating the position of the trapped particle using the centroiding algorithm described in Chapter 4. The position change was converted to real units using the imaging CCD pixel scale given in Table 8. The range of motion results are presented in Table 10.

X axis range of motion (um)	*Y* axis range of motion (um)
+16 um	+ 12 um
- 15 um	- 15 um

Table 10 - Range of trap position in the imaging plane

Currently, range is limited by the wavefront sensor. The focal length of the WFS lenslet's are long enough that, at the limiting range, the centroids move off the CCD causing the controller to fail. Based on equation (27) below, the theoretical range with the current DM and trapping objective was calculated, and is given in Table 11.

$$(x_{max}\,,\, y_{max}) = \pm\frac{fp2}{d} \qquad (27)$$

f	3 mm	Trapping objective effective focal length
P	50 um	Maximum tip/tilt wavefront (manufacture spec)
d	6.75 mm	Diameter of microscope back aperture
x_{max}, y_{max}	**± 22 um**	Theoretical maximum range of trap displacement

Table 11 - Theoretical range of trap position

The theoretical range is ± 22um, approximately 50% further than currently achievable. The ratio of *f* over *d* in equation (27) shows how the range is dependent on the numerical aperture of the microscope objective. However, the 50% unrealized increase in range depends only on the AO system. To attain full range of motion, the wavefront sensor focal length could be reduced 50% from 8mm to 4mm, or the WFS camera could be upgraded to one with a CCD with a minimum area of 4x4 mm^2.

Operating Frequency of the Control System

The AO controller was operated in closed-loop at 20 Hz. The frequency is currently limited by the speed of the control computer. A higher speed AO system could correct the higher frequency air turbulence on the bench, a factor that adds positional variance to the trap. In principle, the AO hardware; DM and WFS CCD, are capable of being operated in excess of 200Hz.

Trap Stiffness using Stokes Flow Based Stiffness Measurement

The trap stiffness was measured using the imaging CCD and centroiding method described in Chapters 2 and 4. As a force probe, trap stiffness should be adjusted to suit the viscoelastic properties of the sample. The simplest method is to change the optical power; hence, the relationship between applied optical power and trap stiffness was measured. The flow velocity was determined by observing the change of position of un-trapped particles during a sequence of video frames. The trap displacement was taken as the average position during these frames, minus the reference position. Flow velocity was converted to applied force using Stoke's law, and plots of force versus displacement were generated. The slope of each plot gives the measured trap stiffness. Note, this method of determining stiffness is independent of the choice of reference position; however, it is affected by the drift of the trap position. The imaging CCD pixel size does not affect trap stiffness, because the same video source is used to measure trap displacement and flow velocity. The distance from the coverslip was measured to be approximately 200 um, or

20 bead diameters. At this distance Faxen's law [1] predicts a negligible change in Stokes drag coefficient, due to the bead's interaction with the coverslip's surface.

Investigating Trap Stiffness as a Function of Optical Power

Trap stiffness was measured at a several optical powers, measured at the back-aperture of the microscope objective. The AO system was activated such that the DM had removed most static aberrations. The experimental parameters and measured trap stiffness are given in Table 12.

Wavelength (nm)	Laser Power (mW)	Bead Diameter (um)	Pixel Scale (um/px)	Range of Flow Velocity (um/s)	Range of Trap Displacements (um)	Trap Stiffness (pN/um)
1064	7.8	10	0.119	.9 – 9	0.1 – 1	**0.776**
1064	12	10	0.119	4.4 – 17	0.1 – 0.90	**1.23**
1064	24	10	0.119	11 – 26	0.15 – 0.54	**2.54**
1064	24	10	0.119	11 – 26	0.15 – 0.54	**2.74**
1064	36	10	0.119	14 – 34	0.37 – 0.73	**3.85**

Table 12 - Experimental parameters and trap stiffness results for various optical powers

Three plots of trapping force-versus bead displacement are shown in Figure 44 through Figure 46. Given the difference in scale, each plot is given separately.

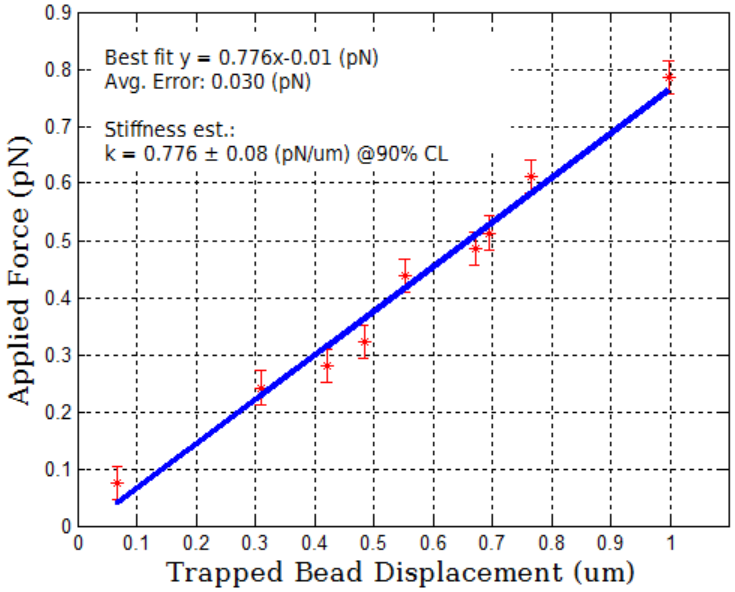

Figure 44 - 7mW - 10um - Applied drag force versus displacement

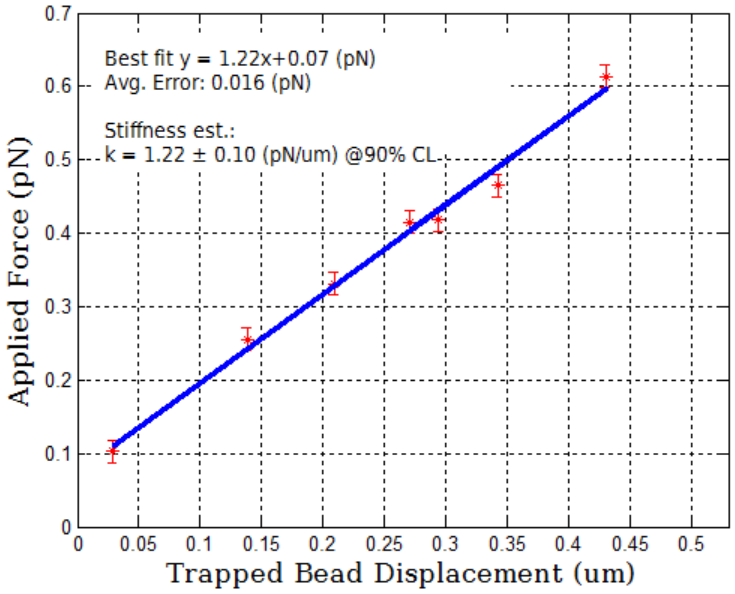

Figure 45 - 12mW - 10um - Applied drag force versus displacement

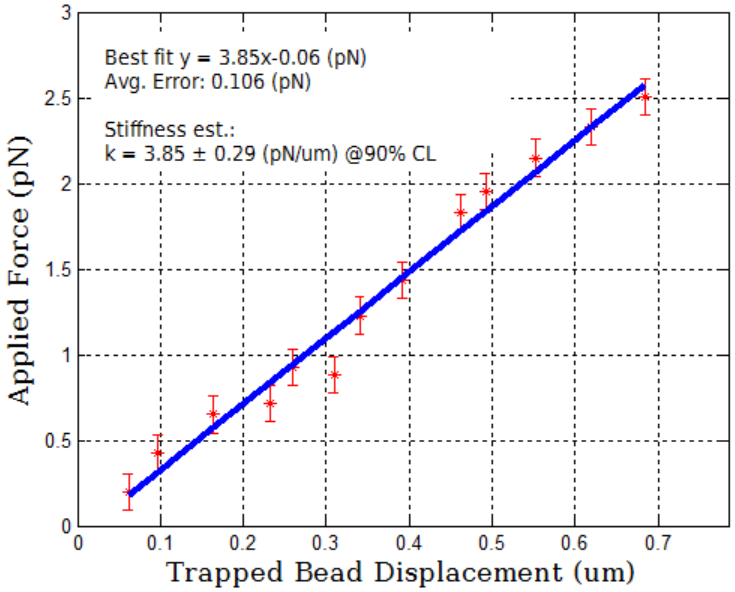

Figure 46 - 36mW - 10um - Applied drag force versus displacement

The magnitude of the error bars, in the above figures, is equal to the standard deviation of the measured values from the best fit line. Using the stiffness values determined above, the plot in Figure 47 shows measured trap stiffness as a function of laser power. As expected, there is a strong linear relationship between optical power and trap stiffness.

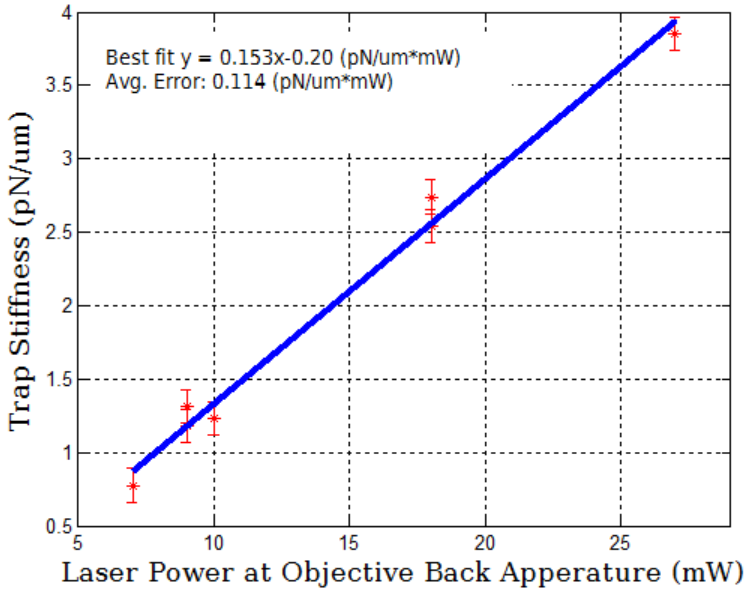

Figure 47 - Trap stiffness at different optical powers. The relationship was found to be highly linear.

Measuring Independence of Trap Stiffness and Trap Position

An experiment was done to determine if there was a noticeable change in stiffness between a bead trapped in the rest position and at a distance offset from the rest position. A large change would require trap stiffness to be mapped at all trap locations to accurately use the tweezer as a force probe. Other research employing wavefront control to manipulate trap position have contradictory findings on its effect on trap stiffness [36][37][21] . In these cases, however, spatial light modulators were used, and the systems did not operate in closed loop with respect to the wavefront shape.

Trap stiffness was determined using the same bead trapped at the rest position and when offset 4 microns in the *x* and *y* direction using the AO system. Later, the experiment was

repeated with the offset changed to the limit of range in the *x* direction. The parameters and stiffness values are given in Table 13.

Trial	Wavelength (nm)	Laser Power (mW)	Bead Diameter (um)	Range of Flow Velocity (um/s)	Range of Trap Displacements (um)	Trap Position (*x*, *y* um)	Measured Trap Stiffness (pN/um)
a	1064	24	10	5 – 14	0.02 – 0.46	0, 0	2.74
b	1064	24	10	6 – 19	0.05 – 0.61	4, 4	2.54
c	1064	12	10	3 – 14	0.13 – 0.89	0, 0	1.31
d	1064	12	10	2 – 13	0.12 – 0.90	14.6, 0	1.18

Table 13 - Trap stiffness and experimental parameters at different trap locations

Plots of trap displacement and applied force are given in Appendix 2 .

Comparing the rest and 4,4um offset cases, the difference in stiffness was 7%. In the rest and x = 15 um offset, the difference was 12%. In both cases, the stiffness was lower at the offset position. However, the difference is less than the stiffness measurement accuracy.

Determining the Trap Position Resolution

The WFS – DM – controller mechanism can move the trap in much finer increments, approximately 10 nm, than can be detected by the imaging system and centroiding algorithm. Detecting trap position is challenging due to random fluctuations in trap position and drifting optical elements. To quantify position detection resolution, the bead position was changed in progressively smaller increments until motion could no longer be detected. This represents the step-size of the bead position monitoring system. In a force

probe, this parameter and the trap stiffness determine the resolution of force application. The results are summarized in Table 14 below.

Minimum detectable WFS command (px)	Peak to peak wavefront tilt at minimum WFS command (um)	Centroid change at minimum detectable WFS command (um)
0.05 px	0.15	**0.067**

Table 14 - Minimum detectable change in bead position by the centroiding method

Linearity between Applied Wavefront Tilt and Trap Displacement

In order to precisely position the optical trap, the AO system assumes trap position changes linearly with the magnitude of applied wavefront tip and tilt. The accuracy of this assumption was investigated by applying successively larger tilts in the *x* and *y* directions, and measuring the corresponding trap position. The difference is termed the positioning error. In an optical trap, the positioning error between the desired and observed trap location limits how well trap position can be controlled. This could limit the precision with which force can be applied and is, therefore, an important factor to measure.

The error has two components: error in observing changes in trap position, and control error. Most of the observation error is due to the mechanical drift of the trapping objective and trap chamber, random thermal motion of the particle, and the centroiding algorithm. The control error reflects how well the AO system is able to change trap position.

The slope of the wavefront produced by DM tip/tilt motions is constant across the beam. This causes the WFS centroids of every lenslet focus to be offset by equal amounts. To create the tip/tilt, the controller's centroid reference positions were changed to include such an offset, in this case 1 pixel *x*,*y*. For each reference, the position of the trapped particle was calculated from the imaging CCD frame. Measurement error was reduced by averaging the calculated trap position across 50 consecutive frames. The reference was changed to four positions of equal spacing. The calculated trap position, as a function of controller command, is given in Figure 48.

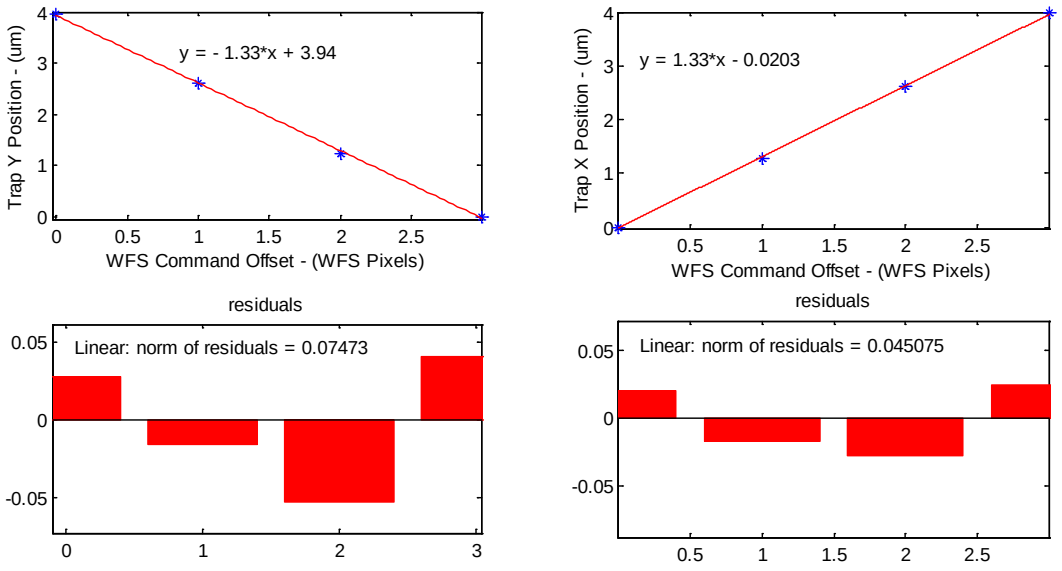

Figure 48 – Top: Measured trap position is shown to follow linearly changes in the controller reference position corresponding to tip/tilt. The slope of the best fit line (red) relates wavefront sensor reference position, *x* in pixels, to trap position in microns. Bottom: The residual error between the best fit line (top), and the measured position, is the positioning error of the trap position control system in um.

On examination of Figure 48, the trap position follows WFS tip/tilt very linearly. This confirms the initial assumption gives good accuracy. A 1 pixel change in WFS reference

was shown to change trap position 1.33 um, or 11.17 pixels on the imaging CCD. In the lower two plots of Figure 48, the difference, or residual, of the trap position measurement compared to the best fit is shown. This is the total positioning error of the apparatus. The norm of the residuals was found to be 0.074 um in the *y* direction, and 0.045 um in the *x*. This is equal to the centroid change at the minimum detectable WFS command, therefore it is due to the imaging system. Another experiment was done using the WFS to detect the minimum observable change in tip/tilt, which was related to trap position using the slope of Figure 48. Based on this result, the minimum command able trap position is estimated to be 0.0011 um, limited by the resolution of the DM electronics. This represents the ideal minimum detectable WFS command; attainable with an optimized bead position measurement system. This corresponds to the positional accuracy reported devices using SLM [21] and AOD [38] technologies.

Chapter 6 – Conclusions and Future Work

Optical tweezers use laser light to trap and manipulate particles that range in size from 100 to 0.1 um. They allow biophysicists to study the mechanical characteristics of bio-molecules and bio-motors with new levels of precision.

This thesis detailed the design and characterization of a unique optical tweezer system. The design features a large reusable aluminum trapping chamber, with a sample holding area 2x6x30 mm in size. The microscope objective used is able to trap a particle at a distance of 2 mm from its front lens, approximately 10x further than a typical optical tweezer. The microscope objective is held at two points along its length, therefore the trap position is less affected by mount vibration.

An adaptive optics system, employing a deformable mirror (DM), control computer, and Shack-Hartmann wavefront sensor (WFS) was designed and implemented to control the wavefront of the optical tweezer system. The system is novel as the controller and DM make continual adjustments to the laser wavefront, based on the WFS measurements. A process of controller calibration was developed to: (i) relate WFS measurements to DM motion, and (ii) relate WFS Zernike modes to trap position.

Control over the *x,y,z* position of the trapped particle was demonstrated using the AO system. The trap position range of motion, in the trapping plane, is approximately 30 um

in the *x* and *y* directions. This is approximately an order of magnitude longer than has been previously demonstrated using DM technologies, due to the large stroke of the DM used in this experiment. An additional 50% of range is estimated to be achievable by doubling the size of the WFS's CCD chip. Utilizing this additional range makes this method comparable to the results obtained using SLM technologies. The minimum observable change in *x,y* trap position is 0.067 um, limited by the imaging system. By optimizing the imaging system, it is believed this could be reduced to 0.0011 um. This corresponds to the accuracy of technologies employing AODs and SLMs.

The resolution of force application of an optical tweezer is dependent on two key measurements: trap stiffness, and trap displacement. The stiffness of the system was calibrated for optical power between 7 and 36 mW measured at the trapping objective's back aperture. Every additional milliwatt of optical power increased trap stiffness by 0.78 pN/um, when trapping a 10 um polystyrene bead. Trap displacement measurement accuracy is negatively affected by drift of the trap location. Drift is caused by small changes in position of the tweezer's optical components, which occur slowly over time. The total drift rate of trap location is approximately 0.125 um / minute. The rate of drift due to movement of optics before the trapping objective is 0.050 um / minute. This component of drift was eliminated using the AO system. The values given are representative of large rates of drift, the absolute speed of which varied considerably throughout experiments.

Future Work

A new upgraded design to improve the optical tweezer system is being pursued. The multi-trap system will enable:

- Trapping of up to four particles down to 0.5 um in diameter using a trapping objective with a greater NA and 4 trap forming micro-lenses.
- Closed-loop manipulation of trap stiffness using the relationship between Zernike wavefront aberrations and the diffraction pattern at the trap focus.
- Elimination of flow due to laser absorption by designing a thinner chamber, enabling the use of higher optical powers and greater trap stiffness
- Improve resolution of trapped particle position using more sophisticated image analysis, and Koehler illumination
- More precise methods of trap stiffness calibration
- Individual *x*,*y*,*z* control of a 2x2 array of trapped particles

Bibliography

[1] Keir Neuman and Steven Block, "Optical trapping," *Review of Scientific Instruments*, vol. 75, no. 9, pp. 2787-2809, September 2004.

[2] Yi-Ren Chang and Long Hsu, "Optical trapping of a spherically symmetric sphere in the ray-optics regime: a model for optical tweezers upon cells," *Applied Optics*, vol. 45, no. 16, pp. 3885-3892, June 2006.

[3] Graham Wright and Jochen Arlt, "Optical tweezer micromanipulation of filamentous fungi," *Fungal Genetics and Biology*, vol. 44, pp. 1-13, 2007.

[4] Arthur Ashkin, "Acceleration and Trapping of Particles by Radiation Pressure," *Physical Review Letters*, no. 24, pp. 156-159, 1970.

[5] S Block, "Optical Tweezers: A new tool for biophysics," *Modern Cell Biology*, vol. 9, pp. 375-402, 1990.

[6] Christoph Baumann et al., "Stretching of Single Collapsed DNA Molecules," *Biophysical Journal*, vol. 78, pp. 1965-1978, April 2000.

[7] Arthur Ashkin and J. Dziedzic, "Optical Trapping and Manipulation of Viruses and Bacteria," *Science*, vol. 235, pp. 1517-1520, March 1987.

[8] B. Maier and I. Chen, "DNA Transport into Bacillus subtilis requires proton motive force to generate large molecular forces," *Nature Structural & Molecular Biology*, vol. 11, no. 7, pp. 643-649, July 2004.

[9] Keir Neuman and Attila Nagy, "Single-molecule force spectroscopy: optical tweezers, magnetic tweezers and atomic force microscopy," *Nature Methods*, vol. 5, no. 6, pp. 491-505, June 2008.

[10] Jordan Zlatanova and Kensal van Holde, "Single-Molecule Biology: What is it and how does it work?," *Molecular Cell*, vol. 24, pp. 317-329, November 2006.

[11] Charles Asbury and Adrian Fehr, "Kinesin Moves by an Aysmmetric Hand-Over-Hand Mechanism," *Science*, vol. 302, no. 5653, pp. 2130-2134, December 2003.

[12] Kishan Dholakia and Peter Reece, "Optical micromanipulation takes hold," *Nanotoday*, vol. 1, no. 1, pp. 18 - 27, Febuary 2006.

[13] Kishan Dholakia and Gabriel Spalding, *SC655 - Introduction to Optical Tweezers and Optical Micromanipulation*. San Diego, USA: SPIE, 2008.

[14] Ciro Cecconi, Elizabeth Shank, and Carlos Bustamante, "Direct Opservation of the Three-State Folding of a Single Protein Molecule," *Science*, vol. 309, no. 5743, pp. 2057-2060, September 2005.

[15] Eric Darlin and Matthew Topel, "Viscoelastic properties of human msenchymally-derived stem cells and pripary osteoblasts, chondrocytes, and adipocytes," *Journal of Biomechanics*, vol. 41, pp. 454-464, June 2008.

[16] Guillaume Lenormand and Sylvie Henon, "Direct Measurement of the Area Expansion and Shear Moduli of the Human Red Blood Cell Membrane Skeleton," *Biophysical Journal*, vol. 81, pp. 43-56, July 2001.

[17] Remus Dame, "Bacterial chromatin organization by H-NS protein unravelled using dual DNA manipulation," *Nature*, vol. 444, no. 7117, pp. 387-390, 2006.

[18] Jacques Beckers, "Adaptive Opticss for Astronomy: Principles, Performance, and Applications," *Annual review of astronomy and astrophysics*, vol. 31, pp. 13-62, 1993.

[19] Peter Glynne-Jones and Rosemary Boltryk, "Flexible Acoustic Particle Manipulation Device with Integrated Optical Wavefuide for Enhanced Microbead Assays," *Analytical Sciences*, vol. 25, pp. 285-291, Febuary 2009.

[20] K. Sasaki and M. Masanori, "Pattern formation and flow control of fine particles by laser-scanning micromanipulation," *Optics Letters*, vol. 16, pp. 1463-146, 1991.

[21] Astrid van der Horst and Nancy Forde, "Calibration of dynamic holographic optical tweezers for force measurements on biomaterials," *Optics Express*, vol. 16, no. 25, 2008.

[22] J. Liesener and M. Reicherter, "Multi-functional optical tweezers using computer-generated holograms," *Optics Communications*, vol. 185, pp. 77-82, November 2000.

[23] Jeffrey Moffitt, Yann Chemla, Steven Smith, and Carlos Bustamante, "Recent Advances in Optical Tweezers," *Annual Review of Biochemistry*, no. 77, pp. 205-228, 2008.

[24] Justin Molloy and Miles Padgett, "Lights, action: optical tweezers," *Contemporary Physics*, vol. 43, no. 4, pp. 241-258, 2002.

[25] Alexander Jesacher and Christian Maurer, "Full phase and amplitude control of holographic optical tweezers with high efficiency," *Optics Express*, vol. 16, no. 7, pp. 4479-4486, March 2008.

[26] Eirini Theofanidou and Laurence Wilson, "Spherical aberration correction for optical tweezers," *Optics Communications*, vol. 236, pp. 145-150, 2004.

[27] Yasuhiro Harada and Asakura Toshimitsu, "Radiation forces on a dielectric sphere in the Rayleigh scattering regime," *Optics Communications*, vol. 124, pp. 529-541, March 1996.

[28] Arthur Ashkin, "Forces of a single-beam gradient laser trap on a bielectric sphere in

the ray optics regime," *Biophysical Journal*, vol. 61, pp. 569-582, Febuary 1992.

[29] Arthur Ashkin and Jason Dziedzic, "Observation of light scattering from nonspherical particles using optical levitation," *Applied Optics*, vol. 19, no. 5, pp. 660-668, 1980.

[30] Zhaohui Hu and Jia Wang, "Manipulation and arrangement of biological and dielectric particles by a lensed fiber probe," *Optics Express*, vol. 12, no. 17, pp. 4123-4128, 2004.

[31] Jean Bennett and Harold Bennett, "Polarization," in *Handbook of Optics*, Walter Driscoll, Ed. New York, USA: McGraw-Hill, 1978, ch. 10, pp. 6 - 10.

[32] Francois Roddier, *Adaptive Optics in Astronomy*. Cambridge, United Kingdom: Cambridge University Press, 1999.

[33] Robert Simmons and Jeffery Finer, "Quantitative Measurements of Force and Displacement Using an Optical Trap," *Biophysical Journal*, vol. 70, pp. 1813-1822, April 1996.

[34] Erwin Peterman and Frederick Gittes, "Laser-Induced Heating in Optical Traps," *Biophysical Journal*, vol. 84, pp. 1308-1316, Febuary 2003.

[35] Li Martin and Jochen Arlt, "Trapping multiple particles in single optical tweezers," *Optical Communications*, no. 281, pp. 135-140, 2008.

[36] F Belloni and S Monneret, "Multiple holographic optical tweezers parallel calibration with optical potential well characterization," *Optics Express*, vol. 16, pp. 9011-9020, 2008.

[37] G Sinclair and G Jordan, "Defining the trapping limits of holographical optical tweezers," *Journal of Modern Optics*, vol. 51, pp. 409-414, 2004.

[38] Megan Valentine and Nicholas Guydosh, "Precision steering of an optical trap by electro-optic deflection," *Optics Letters*, vol. 33, no. 6, pp. 599-601, March 2008.

Appendix 1 Detailed Trapping Chamber Design

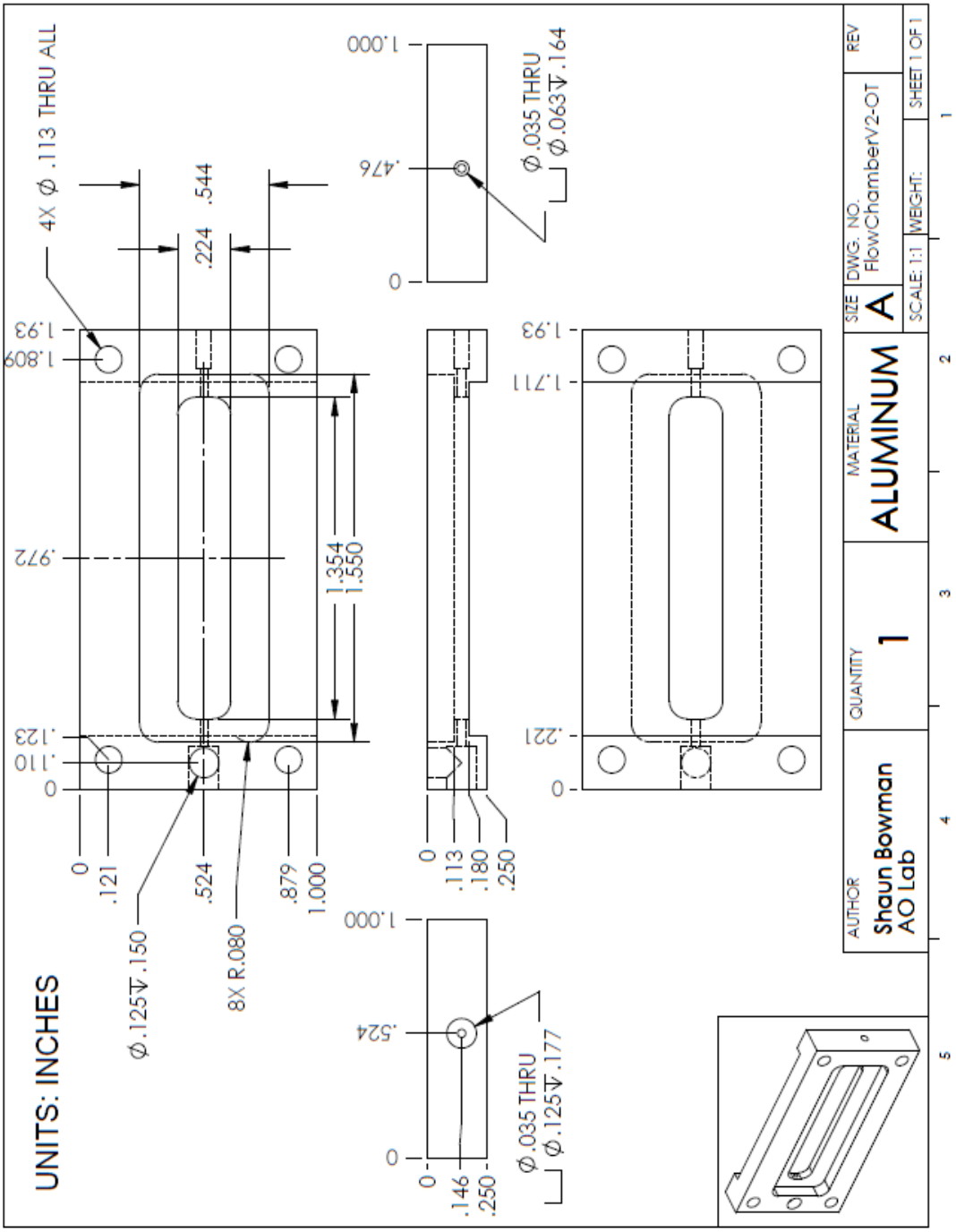

Appendix 2 Experimental Stiffness with an offset beam

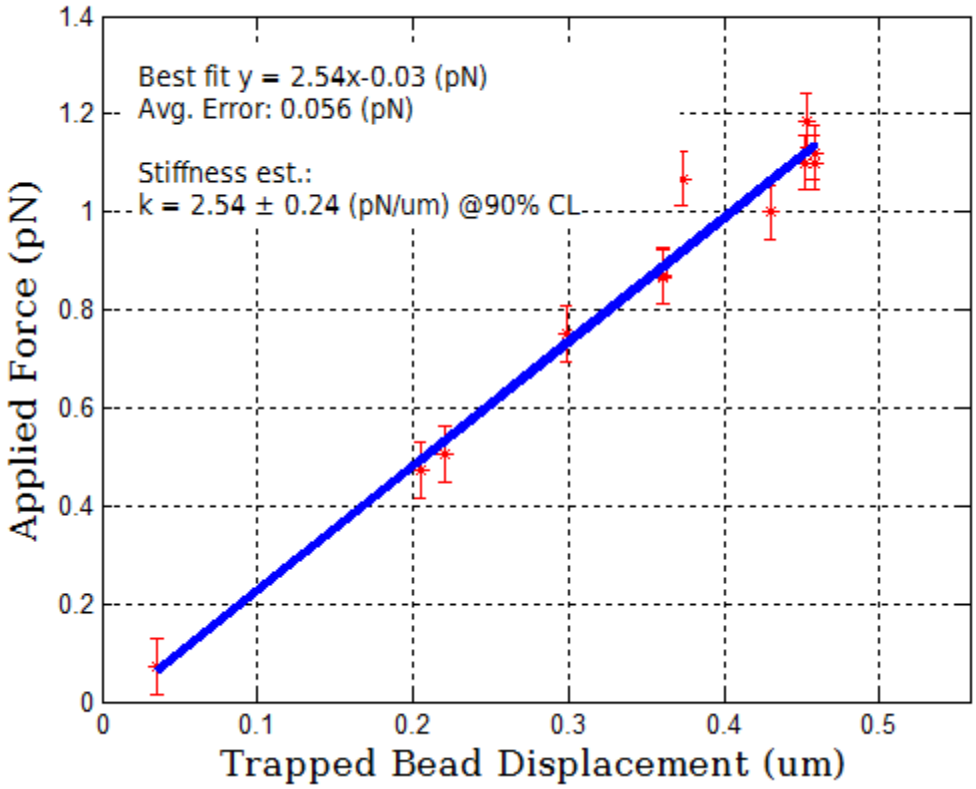

Figure 49 - A 10um bead is trapped approximately 4 um offset from the rest position in directions *x* and *y*. Optical power: 24 mW

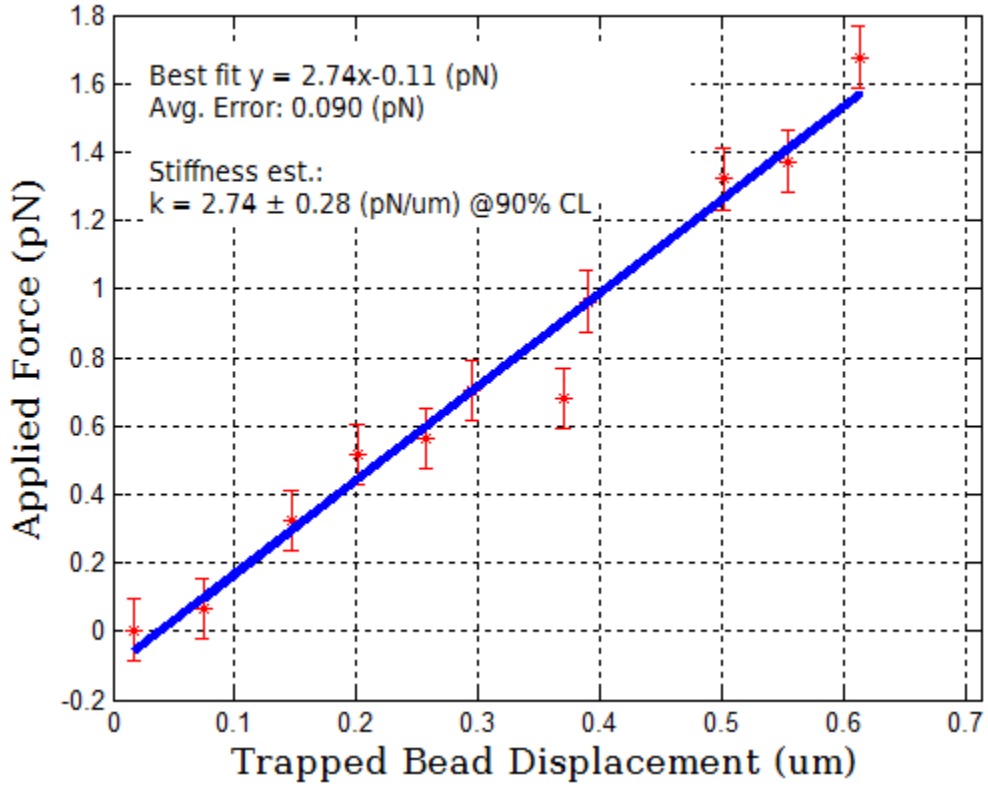

Figure 50 - The same 10um bead used in the 4 um offset scenario was returned to the nominal position and subjected to a similar range of flow conditions. Optical power: 24 mW

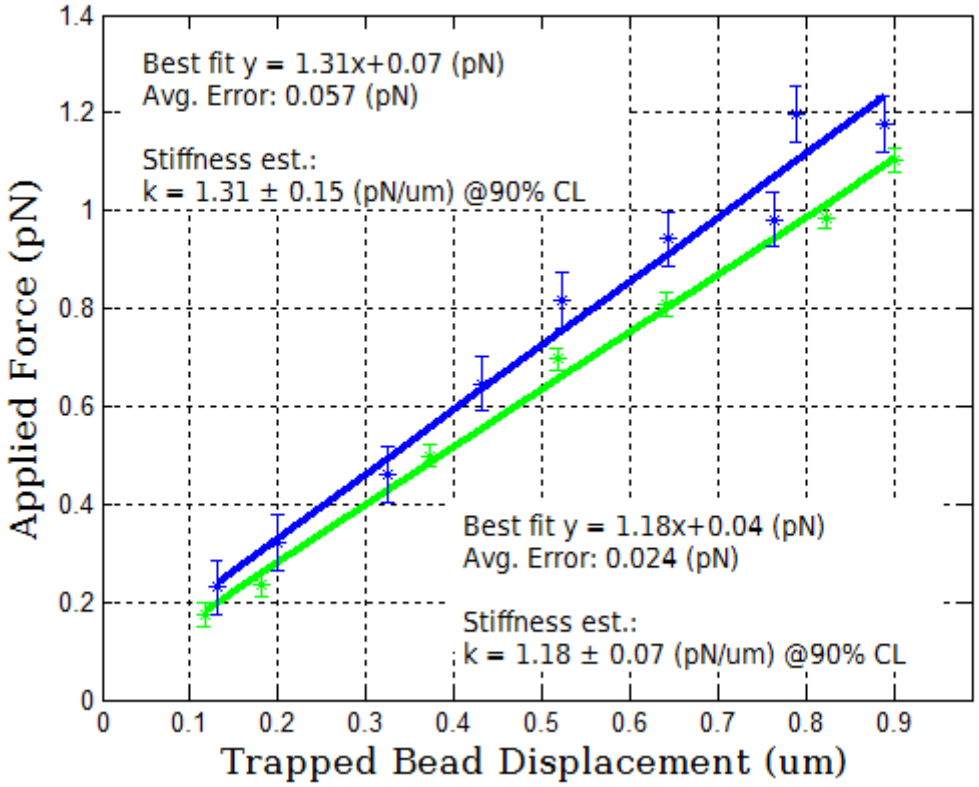

Figure 51 **- Stiffness of a trapped 10 um bead at maximum displacement appliable using the AO system, 15 um (blue), and the stiffness of the same bead at the nominal position. Optical power: 12mW**